LAWRENCE
LIVERMORE
NATIONAL
LABORATORY

LLNL-JRNL-412801

Testing ice microphysics parameterizations in NCAR CAM3 using TWP-ICE data

W. Wang, X. Liu, S. Xie, J. Boyle and S. A. McFarlane

May 5, 2009

Journal of Geophysical Research

Testing ice microphysics parameterizations in NCAR CAM3 using TWP-ICE data

Weiguo Wang[1], Xiaohong Liu[1#], Shaocheng Xie[2], Jim Boyle[2], and Sally A. McFarlane[1]

[1] Pacific Northwest National Laboratory, Richland, Washington, USA

[2] Lawrence Livermore National Laboratory, Livermore, California, USA

[#]Corresponding author contact information,

Xiaohong Liu

Atmospheric Sciences and Global Change Division

Pacific Northwest National Laboratory

Richland, WA 99352

Email: xiaohong.liu@pnl.gov

Abstract

Cloud properties have been simulated with a new double-moment microphysics scheme under the framework of the single column version of NCAR Community Atmospheric Model version 3 (CAM3). For comparison, the same simulation was made with the standard single-moment microphysics scheme of CAM3. Results from both simulations compared favorably with observations during the Tropical Warm Pool – International Cloud Experiment (TWP-ICE) by the US Department of Energy Atmospheric Radiation Measurement (ARM) Program in terms of the temporal variation and vertical distribution of cloud fraction and cloud condensate. Major differences between the two simulations are in the magnitude and distribution of ice water content within the mixed-phase cloud during the monsoon period, though the total frozen water (snow plus ice) content is similar. The ice mass content in the mixed-phase cloud from the new scheme is larger than that from the standard scheme, and ice water content extends 2 km further downward, which are in better agreement with observations. The dependence of the frozen water mass fraction on temperature from the new scheme is also in better agreement with available observations. Outgoing longwave radiation (OLR) at the top of the atmosphere (TOA) from the simulation with the new scheme is in general larger than that with the standard scheme, while the surface downward longwave radiation is similar. Sensitivity tests suggest that different treatments of the ice crystal effective radius contribute significantly to the difference in the calculations of TOA OLR in addition to cloud water path. Numerical experiments show that cloud properties in the new scheme can respond reasonably to changes in the concentration of aerosols and emphasize the importance of correctly simulating aerosol effects in climate models for aerosol-cloud interactions. Further evaluation especially for ice cloud properties based on in-situ data is needed.

Keywords: climate model, cloud microphysics parameterization, mixed-phase clouds, uncertainty, observations

1. Introduction

The cloud system is an essential component of the global climate system. Accurately representing the interaction between clouds and radiation is critical for climate models to simulate the evolution of the global climate system, especially its responses to human activities. Physically, the cloud-radiation interaction depends largely on cloud microphysical properties such as cloud particle size, shape, and number concentration. However, the grid used in climate models is too coarse to fully represent small scale cloud processes. Representation of cloud microphysical processes is oversimplified in many climate models due to the restriction of computation speed and the insufficient understanding of the complex thermodynamical processes inside clouds. This will affect the accuracy of simulated cloud radiative properties in addition to cloud microphysical properties themselves. The formation and evolution of cloud droplets and ice crystals are especially important for mixed-phase clouds because they determine the fraction of the cloud condensate being partitioned to liquid and ice, which significantly affects the cloud and radiation fields and predicted climate changes [*Gregory and Morris*, 1996].

Currently, many climate models are still using single-moment microphysical schemes in which only cloud condensate mass mixing ratios are simulated with prognostic equations. The inability to simulate the responses of important cloud properties such as cloud droplet and ice crystal number concentration to environmental fields has limited the accuracy of the climate simulation and the capability of the model to simulate climate changes in response to aerosols and other chemical components produced by human activities. To address this issue, efforts are being made to introduce prognostic equations for cloud particle number concentration into climate models [e.g., *Liu et al.*, 2007a; *Morrison and Gettelman*, 2008].

In the National Center for Atmospheric Research (NCAR) Community Atmospheric Model version 3 (CAM3), the effective radii of liquid droplets and ice crystals are prescribed or based on empirical relations, rather than calculated directly from prognostic cloud particle mass mixing ratio and number concentration [*Boville et al.*, 2006]. Liu et al. [2007a] introduced a new ice microphysics parameterization to NCAR CAM3 by adding a prognostic equation for ice crystal number concentration. In this new scheme, the effective radius of ice crystals is calculated from their prognostic mass and number concentrations rather than diagnosed from temperature as in the standard CAM3. In addition, the new scheme abandons the assumption that the total cloud condensate is partitioned into liquid and ice parts based only on temperature. The CAM3 with the new parameterization scheme has been evaluated favorably against measurements from the Mixed-Phase Arctic Cloud Experiment [*Liu et al.*, 2007b; *Xie et al.*, 2008]. In these evaluations, most clouds contained a mixture of liquid and ice and appeared within the boundary layer below 2 km. In the current study, the new scheme is applied to tropical clouds during the US DOE ARM (Department of Energy Atmospheric Radiation Measurement Program) Tropical Warm Pool – International Cloud Experiment (TWP-ICE) [*May et al.*, 2008]. To illustrate how microphysical process treatments affect the simulations of cloud condensate of different phases and radiation fields, cloud properties are simulated using a single column model version of CAM3 (SCAM) with the standard cloud microphysics scheme and with the new cloud microphysics scheme, respectively. The TWP-ICE case was selected to evaluate both parameterization schemes for three main reasons. First, numerous observational studies and cloud-resolving simulations in the literature have suggested that tropical clouds play an important role in the global energy budget and water cycle [e.g., *Ecuyer and Stephens*, 2007; *Wu and Moncrieff*, 2001]. As a result, accurately representing tropical cloud microphysical processes is critical. Second, tropical clouds are often multi-layered and complex, appearing from near the surface to the tropopause (about 20 km above the sea level). This provides an excellent scenario to test the new ice parameterization and to show its importance in simulating complex cloud systems. Third, there were intensive observations around the TWP-ICE site (Darwin, 131ºE, 12ºS, northern Australia) through the US DOE ARM program [*May et al.*, 2008]. A ground-based network, aircraft measurements, and flux measurements provided valuable datasets on the scale of a global climate model grid both for forcing SCAM and for comparisons. **Figure 1** shows the observational site and summarizes instrument deployment.

The rest of the manuscript is organized as follows. Section 2 briefly describes the data and standard and modified cloud microphysics schemes used in CAM3. Section 3 presents and discusses the model results. Sensitivity tests are given in Section 4. Section 5 presents a summary of findings from this study.

2 Data and model

2.1 Data

(1) Forcing data

The variational objective analysis approach described in *Zhang and Lin* [1997] and *Zhang et al.* [2001] was used to derive the required large-scale forcing data for SCAM. The basic idea of the analysis approach is to use domain-averaged surface and top of atmosphere (TOA) observations as the constraints to adjust the balloon soundings in order to satisfy the conservation of column integrals of mass, heat, moisture, and momentum. The resulting analyzed data are dynamically and thermodynamically consistent. Input data for the analysis include radiosondes from the 6 sounding stations in the 200 km $\times$ 200 km domain centered at the Darwin ARM site

(**Figure 1**), TOA radiation from Japan's Multi-Functional Transport Satellite, precipitation data from the Australian Bureau of Meteorology's C-band polarization radar, surface radiation from three land stations and one ocean site, surface turbulent fluxes from four land stations, cloud liquid water path (LWP) from microwave radiometer (MWR) and cloud radar, and surface meteorological fields from local stations. For the period when surface flux data are not available, European Centre for Medium-Range Weather Forecasts model (ECMWF) analysis data, which are adjusted using the linear regression equation derived during the times when both ECMWF and observations are available, are used. The analysis data cover the period from 03:00 UT 19 January to 21:00 UT 12 February 2006. Details about the analysis can be found in the paper by *Xie et al.* [2009].

(2) Liquid and ice water data from ARM cloud radar

Cloud microphysical information is retrieved primarily from the ARM 35 GHz micrometer cloud radar (MMCR) based on observed reflectivity, as described in *Mather et al.* [2007]. Based on aircraft in situ data that shows liquid water is rarely found in tropical clouds below -16 ºC except near core updraft regions [*Stith et al.*, 2004], the retrieval process assumes that all cloud water is liquid for temperature above 0 ºC, ice for temperature below -16 ºC, and mixed phase at intermediate temperatures. For the mixed phase regions, the fraction of radar reflectivity associated with ice increases as a linear function of decreasing temperature. For liquid clouds or liquid part of the mixed phase clouds, the regression equation by *Liao and Sassen* [1994] is employed to estimate liquid water content (LWC) from radar reflectivity, assuming a number concentration of 100 cm^{-3}. The resulting LWC is scaled to match LWP measurements from MWR during non-precipitating conditions. For ice clouds or ice part of the mixed-phase clouds, ice water content (IWC) is calculated with the empirical relation proposed by *Liu and Illingworth* [2000].

Uncertainties in the current retrieval are estimated to be from -50% to 100% in IWC and -10% to 10% in LWC for non-precipitating clouds [*Mather et al.*, 2007]. *Comstock et al.* [2007] compared about 10 different retrievals of mid-latitude, non-precipitating ice cloud properties in a case study and found factors of 2-3 differences in the ice water path (IWP) and optical depth. Uncertainties are higher for the mixed phase and precipitating periods because the relations used were not developed for these scenarios [*Mather et al.*, 2007] and during precipitating periods the MMCR signal may be attenuated by the precipitation (i.e., IWC above precipitating clouds may be underestimated). The MMCR cannot detect all cirrus at tropical sites and usually miss thin cirrus with bases above 15 km due to a combination of decreased sensitivity with increasing range from the radar and the presence of small crystals in these thin cirrus [*Comstock et al.*, 2002]. Prior to the TWP-ICE experiment, the MMCR was damaged by a lightning strike, resulting in a loss of sensitivity of 10-15 dB relative to normal operations, further reducing the sensitivity to high cirrus. The LWC and IWC retrievals are performed every 5 minutes at 45-m vertical resolution and are averaged and regridded to match the time and vertical resolution of the variational forcing dataset.

(3) ARSCL cloud fraction

During TWP-ICE, hydrometeors (clouds) were observed by the ARM radars and other remote sensors including a micropulse lidar. The vertical distribution of the frequency of occurrence of hydrometeors (clouds) is estimated by combining those measurements using the active remotely sensed cloud locations (ARSCL) algorithm described by *Clothiaux et al.* [2000].

Measurements from cloud radars have several limitations. First, the cloud base detected by the cloud radar can be contaminated by ice precipitation as the radar is more sensitive to large precipitation particles than to smaller cloud particles. To address this problem, the cloud base is estimated from measurements of the ARM laser ceilometer and micropulse lidar that can measure the cloud base more accurately. However, during very strong precipitation, even these instruments may underestimate cloud base. Second, the cloud radar tends to miss high-altitude clouds and underestimate the cloud top height due to the sensitivity of the radar decreasing with distance. Including the lidar in the ARSCL algorithm improves the detection of thin cirrus, although the lidar may be attenuated by thick clouds or precipitation underlying the cirrus. Third, the radar's lower-altitude data are often contaminated with echoes from nonhydrometeor targets such as birds and insects, although the ARSCL processing removes much of this noise. Despite those limitations, radar observations still provide valuable information about the vertical distribution of clouds.

(4) IWC retrieved from satellite observations

Three-dimensional cloud ice water content distribution over the $10^{o}\times10^{o}$ area centered near the Darwin site is retrieved by combining ground cloud radar and satellite high-frequency microwave measurements [*Seo and Liu*, 2005; 2006]. For the TWP-ICE case, measurements from 4 satellites (NOAA-15, -16, -17,-18) are used. We averaged the retrieved data over the 200 km $\times$ 200 km area centered at the Darwin site for comparison with SCAM results. According to theoretical calculations, the first quartile, median, and third quartile values of the uncertainties in IWC retrievals are 37%, 60%, and 112%, respectively.

2.2 Standard CAM3

The NCAR CAM3 is an atmospheric general circulation model [*Collins et al.*, 2006]. The deep convection parameterization is based on the work by Zhang and McFarlane [1995]. The treatment of cloud microphysics and condensate is based on the formulation proposed by Rasch and Kristjánnson [1998] with modification by Zhang et al. [2003]. Although ice and liquid water mixing ratios are simulated by two separate prognostic equations, the total cloud condensate is repartitioned each time step after advection, convective detrainment, and sedimentation processes. The partition of the total condensate into liquid and ice phases is based on temperature. The fraction of ice water (f_{ice}) in the total condensate is estimated simply by,

$$\begin{array}{ll} f_{ice} = 1 & for\ T < T_{\min} \\ f_{ice} = (T_{\max} - T)/(T_{\max} - T_{\min}) & for\ T \in [T_{\min}, T_{\max}] \\ f_{ice} = 0 & for\ T > T_{\max} \end{array} \quad (1)$$

where T is air temperature in ºC, T_{min} and T_{max} are prescribed temperature values, which are -40 ºC and -10 ºC, respectively. This means that mixed-phase clouds exist only between -40 ºC and -10 ºC. The layered cloud fraction (f_c) is diagnosed empirically from relative humidity (RH),

$$0 \le f_c = \left(\frac{RH - RH_{\min}}{1 - RH_{\min}} \right)^2 \le 1, \quad (2)$$

where RH_{min} is a threshold depending on pressure, RH is calculated with respect to water saturation for T > 0 ºC and with respect to ice saturation for T < -20 ºC. For T between -20 ºC and 0 ºC, RH is calculated with respect to a value that is linearly interpolated between the ice saturation and the water saturation. Details for the standard CAM3 can be found in the paper by *Collins et al.* [2006].

2.3 CAM3 with a double-moment ice microphysical scheme

Major changes to the standard CAM3 are highlighted here. Readers are referred to the manuscript by *Liu et al.* [2007a] for details. Two prognostic equations are introduced to CAM3, one for the droplet number concentration, and the other for the ice number concentration. The droplet number equation includes source terms of droplet nucleation, detrainment of convective condensates, and melting of ice crystals, and loss terms of evaporation of droplets, freezing of droplet to ice crystals, autoconversion of cloud droplets to rain droplets, and accretion of cloud droplets by rain and snow. Because *Liu et al.* [2007a]'s scheme and this study focus on ice microphysics, the aerosol effects on liquid water clouds are turned off and the cloud droplet effective radius (r_{el}) and number concentration (N_{d}) are prescribed as in the standard CAM3 for liquid cloud microphysics and radiation calculations. r_{el} is prescribed to be 14 μm over oceans, while it is a function of temperature and snow depth over land. For $T > 0$ °C, r_{el} is assumed to be 8 μm over land in the absence of snow and ramps linearly toward the pristine value of 14 μm as water equivalent snow depth over land goes from 0 to 0.1 m [*Boville et al.*, 2006]. N_{d} is prescribed to be 400 cm^{-3} over land near the surface, and 150 cm^{-3} over the ocean.

The ice number concentration can be changed due to microphysical processes including the nucleation of ice crystals, cloud droplet freezing, the secondary production of ice crystals, the aggregation of ice crystals to form snow, accretion of ice crystals by snow, and melting of ice crystals in addition to advection, turbulent diffusion, and convective detrainment. The ice number concentration change rate due to detrainment is parameterized as $3\rho Q/(4\pi\rho_i r_v^3)$ [*Lohmann*, 2002], where ρ is the air density, Q is the detrainment rate of cloud water mass from the deep convection parameterization, r_v is the volume mean radius of ice crystals and is determined from a temperature-dependent lookup table as used in the standard CAM3 [*Boville et* *al.*, 2006]. Because ice nucleation requires supersaturation, the saturation adjustment [*Rasch and Kristjánsson*, 1998; *Zhang et al.*, 2003] is only applied for liquid clouds and vapor deposition on ice is added for ice clouds. While Eq. (2) is still used to estimate cloud fraction except that ice supersaturation is allowed in the upper troposphere, the repartitioning process based on Eq. (1) is abandoned by explicitly considering the liquid conversion to ice in the mixed-phase clouds through the Bergeron-Findeisen process [*Liu et al.*, 2007a]. The liquid mass conversion to ice due to the deposition growth of cloud ice at the expense of liquid water is based on the scheme proposed by *Rotstayn et al.* [2000], which accounts for the dependence of vapor deposition on crystal size. Ice nucleation mechanisms in *Liu et al.* [2007a] include homogeneous ice nucleation on sulfate particles and heterogeneous immersion nucleation on soot and mineral dust particles in ice clouds with temperature less than -35 ºC [*Liu and Penner*, 2005], contact freezing of cloud droplets through Brownian coagulation with insoluble ice nuclei (assumed to be supermicron mineral dust) [*Young*, 1974], and deposition/condensation nucleation [*Meyers et al.*, 1992] in mixed-phase clouds. Secondary ice production by ice splintering between -3 and -8 ºC is included using the Hallet-Mossop scheme. The Meyers et al. (1992)'s formula is scaled with a vertical decay function obtained for refractory aerosols in the aircraft campaigns for the project of interhemispheric differences in cirrus properties from anthropogenic emissions [*Minikin et al.*, 2003].

Another feature of the modified scheme is that the ice crystal effective radius is calculated as a function of the predicted ice crystal mass and number concentration, rather than as a function of temperature in the standard CAM3. This makes the model respond more sensitive to changes in cloud microphysical properties through radiation calculations. The aerosol climatology prescribed in the CAM3 is used for this study, which was derived from a chemical transport model constrained by assimilation of satellite retrievals of aerosol optical depth for the period of 1995-2000 [*Collins et al.*, 2001; *Rasch et al.*, 2001]. Aerosol measurements from the TWP-ICE campaign are not available. We compared CAM3 aerosol with aircraft measurements below 4 km from the Aerosol and Chemical Transport in tropIcal conVEction (ACTIVE) aircraft campaign [*Allen et al.*, 2008] in the same region during the time period of this study. Sulfate mass concentrations from the ACTIVE aircraft measurements are available below 4 km, which are averaged from surface to 4 km to be 1.71 and 0.42 μg m^{-3} for the monsoon and suppressed periods, respectively. The much higher sulfate concentration during the monsoon period is supposed to be due to sulfate aqueous phase production in clouds [*Allen et al.*, 2008]. Sulfate concentrations from CAM3 monthly climatology range between 0.1 and 0.2 μg m^{-3} from the surface up to 4 km during our simulation period. Sulfate influences the homogeneous nucleation below -35ºC, which is unlikely to play an important role for the mixed-phase clouds during the monsoon period. However, sulfate particles can be important cloud condensational nuclei for droplet formation. Therefore, we have made sensitivity tests (Section 4.4) to examine the effects of cloud droplet number and size on model results. Soot concentrations from the CAM3 aerosol climatology data range between 0.005 and 0.02 μg m^{-3} from the surface to 4 km, which are close to the ACTIVE measurements (0.04 μg m^{-3} during the monsoon period and below the detection limit of 0.01 μg m^{-3} during the suppressed period). Mineral dust measurements are not available from the ACTIVE campaign. To address the effects of uncertainty in the dust concentration adopted from the CAM3 aerosol climatology data, additional sensitivity tests have been designed by varying the rate of contact ice nucleation in which dust particles act as ice nuclei in Section 4.4.

2.4 Model integration

A series of 36-hour simulations with SCAM are initialized at 1200UT of every day for the entire TWP-ICE period from 19 January to 12 February, 2006 to avoid serious drift of SCM simulation. A composite of 12-36 hour forecasts from the series of 36-hour runs is analyzed to reduce model spin-up/spin down problem. Large-scale vertical motion field and horizontal advective tendencies of water vapor and temperature are specified by the derived forcing data as mentioned in section 2.1. It should be noted that large-scale advection of cloud condensate is not provided in the forcing data. As a result, all the model-calculated condensate is generated by cloud microphysical processes.

3 Model Results and discussion

In this section, we will briefly describe the meteorological conditions during the simulation period. Then, SCAM-generated cloud properties will be evaluated against TWP-ICE observations.

3.1 Overview of weather conditions

The synoptic conditions during TWP-ICE have been summarized in *May et al.* [2008]. The weather during TWP-ICE can be divided into three periods, i.e., the monsoon period (13 to 25 January, 2006), suppressed period (26 January to 3 February), and break period (4 to 13 February). During 19-25 January 2006, tropical cyclone Daryl formed off the western Australian coast, moved to the southwest, and weakened over the Indian Ocean. A Low pressure system formed in the Solomon Sea and moved west. This system reactivated monsoon weather on 24 and 25 January. During 26-31 January, the monsoon low pressure system moved inland and deepened, with strong westerly wind at the Darwin site. During the period of 3-13 February, the monsoon dissipated in the Australian region and an inland heat trough dominated across north Australia. **Figure 2** shows the time series of the precipitation rate. Major precipitation occurred until 00:00 UT (=09:00 local time) on 25 January. Light precipitation was observed during other periods. Starting from 7 February, the Darwin site was affected by deep continental storms, with rainfall increasing until 13 February. This period is not included in the following analyses, which focus on the monsoon period and the subsequent suppressed period. **Figure 2** also shows that the precipitation rates from the standard SCAM (SCAM_std) and SCAM with the new ice parameterization (SCAM_new) are in good agreement with MWR observations. This indicates that both models are capable to capture those precipitation events that occurred during the two periods.

Figure 3a shows the time-height cross section of the ARSCL-derived frequency of the occurrence of clouds, indicating the evolution of deep and multilayer clouds in the Darwin area. Not surprisingly, the occurrence of clouds is closely correlated with synoptic scale weather conditions as described above. During the monsoon period, clouds are distributed from the boundary layer top up to 15 km due to strong convection and moisture advection by the westerly flow from the ocean. During the suppressed period of 25 to 30 January, extensive boundary layer clouds with the cloud top of about 2 km and persistent high-level cirrus are observed. After 30 January, scattered boundary layer clouds, middle- and high-level clouds are observed. The ARSCL data also suggest that the moist deep convection occurs mostly during the monsoon period while only occasionally during the suppressed period.

3.2 Cloud fraction

It is necessary to compare model simulations with observations for evaluation. Such comparisons, however, are difficult because meteorological variables output from SCAM represent their averages over a GCM grid size on the scale of 200 km, while radar and lidar measurements represent a single point. To improve the representation of point measurements over a large area, we averaged observations over three hours then compared them with SCAM results. The representativeness of such an average of point measurements depends on the wind conditions and the isotropy of the large-scale cloud field. Satellite retrievals provide area-averaged cloud properties only when satellites pass the experimental site. Thus, the temporal resolution of satellite observations is lower than radar observations. The accuracies of both radar and satellite retrievals are dependent on the retrieval algorithms used as well as the sensitivities of the instruments. Despite the mismatches of temporal and spatial scales between model simulations and observations, it is still useful to qualitatively evaluate model results with these observations.

Figure 3b and 3c show the time-height distributions of cloud fraction simulated by SCAM_std and SCAM_new, respectively. Compared to the ARSCL clouds, both runs reproduce deep and multilayered clouds during the monsoon period and high- and low-level clouds during the suppressed period. Cloud top for high-level clouds simulated by both SCAM runs tend to be higher than that from the ARSCL observations for the entire period; this is partially due to the fact that the cloud radar's sensitivity is reduced with height and usually misses some high-level clouds. Another possibility is that both SCAM runs likely overestimate cloud fraction because early studies have showed that the NCAR CAM tended to overestimate high-level cloud fraction in its short-range weather forecast and climate simulations [*Boyle et al.*, 2005; *Xie et al.*, 2004; *Zhang et al.*, 2005]. This overestimation is further degraded by the SCAM_new run in which ice supersaturation is allowed and the same value for the parameter $RH_{\min}$ in Equation (2) is used [*Liu et al.*, 2007a].

For the monsoon period of 20-25 January, cloud fraction simulated from each run is lower than that from ASRCL retrievals below 5 km but higher above 5 km. The difference in cloud fraction below 5 km may be due in part to difficulty in accurately determining cloud base from the remote sensors in heavily precipitating conditions. In these cases, retrieved cloud base may be too low. For levels above 5 km where the temperature is below the freezing point, cloud fraction from the SCAM_new run is larger than that from the SCAM_std run; this is in part because supersaturation with respect to ice is allowed in the new parameterization [*Liu et al.*, 2007a]. For the same reason, the SCAM_new run produces thicker high-level cirrus clouds and larger cloud fraction than the SCAM_std run during the suppressed period. It is noticed that the distributions of cloud fraction shown here and cloud condensate to be discussed later are not consistent; this is because CAM3 cloud fraction is estimated by the simulated large-scale relative humidity rather than cloud condensate. Addressing this issue is desirable in the future. Additionally, there is inconsistency in the observed fields since cloud condensate retrievals are performed only for radar detected clouds, while cloud fraction in the ARSCL product includes radar and lidar detected clouds.

During the suppressed period, both runs generate extensive and thick low-level warm clouds (below 5 km) and middle-level clouds. This is somewhat inconsistent with radar and lidar retrievals showing that boundary layer clouds are located at about 2km and nearly no middle-level clouds exist. The base height (~12 km) of high-level clouds simulated from each SCAM run is in good agreement with that indicated from ARSCL retrievals. High-level cloud fraction and depth, however, are larger than those suggested from ASCRL retrievals. Such inconsistency is partially attributed to the limitation of radar measuring high-level clouds. In addition, we suggest that the overestimated cloud fraction might be partially due to simulated deep convection being too active. We examined the Zhang-McFarlane (ZM) deep convection [*Zhang and McFarlane*, 1995] output from each SCAM run and found that the ZM deep convection process in the model is activated (triggered) more frequently than that suggested from the ASCRL data. This is a well-known problem with the ZM scheme as illustrated in previous studies [*Boyle et al.*, 2005; *Xie and Zhang*, 2000].

3.3 Liquid water content (LWC) and Liquid water path

Figure 4 shows the time-height cross-sections of LWC from both runs. During the monsoon period, liquid cloud water with LWC > 0.5 mg m^{-3} is distributed from near the surface to nearly 12 km, with most being found between 3 and 9 km (the layer with temperature approximately between -30 and 10 ºC). Differences in LWC from the two runs mostly appear during this period. On average, clouds simulated from SCAM_std contain more liquid water than those from SCAM_new above 6 km, while less between 3 and 6 km. During the suppressed period, LWC distributions simulated from both SCAM runs are in good agreement with radar observations in terms of height and magnitude. Since only minor precipitation occurs during this period, radar observations are more reliable than those during the monsoon period. Most of the cloud liquid water simulated from both SCAM runs appears below 2 km (**Figure 4**). Both SCAM runs produce liquid cloud water at middle levels (5 km), for example, during the periods of 26, 29 January, and 1 February, similar to radar observations. It is noticed that the SCAM_std run produces a small amount (0.5-5 mg m^{-3}) of liquid cloud water appearing near 12 km above the ground even during the suppressed period, which is unlikely to be realistic, while the

SCAM_new run does not. In situ aircraft observations indicate that most tropical clouds glaciate rapidly and supercooled cloud water is rarely seen in the tropics at temperatures below -16 °C except near the core regimes of updrafts [*Stith et al.*, 2004].

Figure 5 shows the time series of the cloud LWP simulated from the SCAM_std and SCAM_new runs and LWP retrieved from MWR. Large LWP differences between the two runs appear during the monsoon period when ice water coexists with liquid water in the mixed phase clouds, with LWP simulated by SCAM_std being up to 30-100% larger than that by SCAM_new before 22 January. This is a result of different treatments of ice microphysics parameterization. In contrast, LWP differences are small during the suppressed period because most of liquid water is from low-level warm clouds, where the new ice scheme has little impact. Because radar and MWR retrievals are rather uncertain when precipitation occurs (during most hours of the monsoon period), we quantitatively compared LWP from models with those from MWR retrievals only during the non-precipitating (precipitation rate from the ground-based observations < 0.2 mm hr^{-1}) hours (Table 1). The LWP values from both SCAM_new and SCAM_std runs are larger than the MWR result during the monsoon and suppressed periods, but the former tends to be closer during the monsoon period.

3.4 IWC and IWP

Figure 6 shows the time-height cross-section of the frozen water (FW, ice plus snow) mixing ratio. Inclusion of snow is for comparisons with observations because the satellite and radar retrieval algorithms are not able to separate snow from ice. FW distributions from both runs are in good agreement with those from satellite retrievals in terms of temporal variation, vertical distribution, and magnitude. During the monsoon period, the lowest height of the FW distribution from each SCAM run is at about 4.7 km, compared to 5.2 km from satellite retrievals and 4.6 km from radar retrievals. FW distributions from both SCAM runs extend to higher levels than those from satellite retrievals. During the suppressed period, the base height of the FW distribution (with the mixing ratio ≥ 1 mg m^{-3}) aloft from each run is in good agreement with that of radar retrievals, though the depth is thicker partially due to the fact that the radar may miss high-level thin clouds. The larger temporal variability and peak value of the radar-retrieved FW mixing ratio are likely because radar retrievals are from measurements at a single point while model results are averaged over a grid. Between the two simulations, FW from the SCAM_new run is generally larger than that from the SCAM_std run above 6 km during the monsoon period, and closer to satellite retrievals. During the suppressed period, both runs produce similar FW distributions at middle and high levels.

Figure 7 compares the model-generated ice water path (IWP) values with satellite and radar retrievals. Note that the contribution of snow has been included into the IWP calculation for comparison with observations. Both SCAM runs generally capture the temporal variation of IWP (e.g., the maxima in 23 and 24 January), compared to satellite retrievals. During the non-precipitating hours of the suppressed period, the model-calculated IWP values from both runs are larger than cloud radar and satellite retrievals, with IWP from SCAM_new being closer to the retrievals than that from SCAM_std (Table 1). During the monsoon period, the IWP values from both runs are similar to the satellite retrievals (within one standard deviation). For the non-precipitating hours of the monsoon period, the IWP values from both runs are larger than the radar and satellite retrievals.

While the magnitude and distribution of the FW mixing ratio between two SCAM runs are similar, the ice mass fraction out of the FW from the SCAM_std run is significantly smaller than that from the SCAM_new run during the monsoon period and slightly larger during the suppressed period. This is a result of different ice microphysics for the mixed-phase clouds: the SCAM_std employs a temperature-dependent function to partition total cloud water into liquid and ice while the SCAM_new explicitly calculates the liquid conversion to ice through the Bergeron-Findeisen process. In light of the important role of ice cloud water in the radiation calculation (snow effects have been ignored in NCAR CAM3), **Figure 8** shows the time-height distributions of cloud IWC simulated from both runs. Similar to LWC, significant differences in IWC are marked for the mixed-phase clouds during the monsoon period in two aspects as highlighted in **Figure 9**. First, the base level of the ice cloud water distribution simulated by SCAM_std is about 7 km which is the height at which the temperature is lower than -10 ºC and ice water can exist according to the temperature-dependent partitioning assumption (see Eq.1). In contrast, the IWC base height is 5 km from the SCAM_new run, 2 km lower than that from the SCAM_std run. Second, SCAM_new produces up to 100 mg m^{-3} more IWC than SCAM_std, especially between 5 and 12 km (see **Figure 8**). The vertical distribution and magnitude of frozen water from the new scheme are closer to satellite retrievals than those from the standard scheme (**Figure 9**), though differences still exist. Different distributions and magnitudes of ice water may affect the simulated radiation and atmospheric heating rate because the optical properties of ice and liquid water are different.

3.5 Ice mass fraction inside mixed-phase clouds

A major difference between the two SCAM runs is the treatment of partitioning of cloud condensate into liquid and ice water components as discussed in section 2. We constructed a joint frequency distribution of temperature and frozen water mass fraction (f_{ice}) in total cloud condensate during the monsoon period for each run (**Figure 10**). Snow mixing ratio has been included in the ice phase for comparisons with observations. Ice mass fraction data, excluding those smaller than 0.01 or larger than 0.99, are binned starting from 0 to 1 with an increment of 0.1. Temperature data are binned starting from -40 to 10 ºC with an increment of 2 ºC. The frequency distribution is constructed by counting the number of data points over each bin and then normalizing by the total number of data points.

Results from both SCAM runs exhibit large variability of ice mass fraction for a given temperature. f_{ice} varies from 0 to 1 when temperature nears 0 º*C*, and increases with decreasing temperature. Liquid water can be present down to -37 ºC and ice water up to a few degrees above 0 ºC (which is precipitating snow). However, the ice mass fraction from the SCAM_std run is smaller than that from the SCAM_new run for a given temperature in most cases. The latter is closer to field observations from mid-latitude clouds by *Field et al.* [2005]. This suggests that the prescribed temperature-dependent partitioning relation in the standard CAM3 may underestimate the fraction of cloud condensate converted to ice; this is improved by applying the new ice parameterization assuming that ice mass fraction is similar in tropical and mid-latitude clouds. It is noted that the red curve shown in Figure 10a is not a straight line, while the ice mass fraction has been assumed to vary linearly with temperature (Eq (1)). This is because the snow has been included in the ice mass in Figure 10.

3.6 Radiation fields

Clouds impact the atmospheric radiation balance by absorbing and scattering shortwave radiation and absorbing and emitting longwave radiation. However, it is not easy to compare grid-mean results from models with point measurements, especially those observed by the coast stations used in TWP-ICE. As discussed in *Xie et al.* (2008), shortwave radiation can be significantly affected by surface characteristics that may not be well represented in a CAM3 grid box. In contrast, the outgoing longwave radiation (OLR) at TOA and surface downward longwave radiation (SDLR) are less affected by surface characteristics. Therefore, they are selected for evaluation. The magnitude of TOA OLR is generally dependent on cloud macrophysical properties such as cloud amount and altitude (temperature), and on microphysical properties of clouds including optical depth and particle size.

Figure 11(a) shows the time series of TOA OLR from both SCAM runs and from satellite retrievals. Both SCAM runs can reasonably capture the temporal variability of TOA OLR. However, the simulated TOA OLR tends to be consistently larger than satellite retrievals, especially during 25-30 January of the suppressed period. This can be partially explained by the following two reasons. First, the temperature around 100 hPa estimated from both simulations is found to be 3 ºC higher than that from the radiosonde data (figure not shown). Second, the inconsistency in TOA OLR between the model output and satellite retrieval may be partially due to uncertainty in satellite retrievals. We compared the cloud thickness derived from ARSCL and satellite retrievals, and found that the satellite retrieval is significantly larger than the ARSCL data during the suppressed period; this suggests that the satellite retrieval likely underestimates TOA OLR.

It is interesting to find that TOA OLR from the SCAM_new run is larger than that from the SCAM_std run in many cases, though the cloud fraction is larger. This can be explained by different cloud top height and optical depths. For example, during 23-25 January of the monsoon period, the cloud top (cloud water mixing ratio is equal to 10^{-3} g m^{-3}) and cloud water path in the SCAM_new run are lower than those in the SCAM_std run, and the temperature of cloud top is higher, resulting in higher TOA OLR values from the SCAM_new run. During the suppressed period, the optical depth of high-level clouds is slightly thinner in the SCAM_new run; this may partially contribute to its higher TOA OLR. Another possible reason is due to the different ice effective radius formulations adopted in the two simulations. Cirrus clouds in the SCAM_new run are found to have larger effective radius values than in the SCAM_std run during the suppressed period, suggesting that SCAM_new's cirrus clouds are more transparent to the longwave radiation below them than SCAM_std's. This can explain approximately 50% of the differences in TOA OLR between the two simulations according to an experiment described in section 4.

Figure 11 (b) shows the time series of SDLR. Surface radiation measurements are made from 3 land stations and 1 ocean station. For comparison, they are averaged over the 200 km × 200 km domain centered at the Darwin site with a weight of 0.57 for land and 0.43 for ocean data. It is found that both SCAM runs capture the temporal variability of SDLR, as for TOA OLR. Overall, SDLR from each SCAM run is larger than that from surface observations. This is consistent with the likely overestimation of low level cloud fraction and LWC as indicated from previous sections. The magnitude of SDLR is closely related to cloud base altitude (and hence temperature) and cloud water amount. Differences in these two variables can explain differences among model results and observations (see **Figure 4**). For example, for the one-day period from the midday of 25 January, both SCAM runs generate larger cloud fraction values than observations at 1-2 km and lower cloud base altitudes, resulting in larger SDLR values. The SCAM_new run generates a smaller LWC than SCAM_std, and hence a smaller SDLR, which is closer to observations.

4. Sensitivity tests

Studies have shown that cirrus clouds, though they are optically thin and contain low water content, may not only affect shortwave radiation but also affect longwave radiation because of their high altitude [*Delamere et al.*, 2000; *Iacobellis et al.*, 2003; *Kristjánsson and Kristiansen*, 2000]. The effective radius (r_{ei}) of ice particles is an important parameter representing radiative properties of ice clouds and gravitational settling of ice particles in NCAR CAM3 as well as in many other climate models. Ice absorption in the longwave radiation decreases with increasing particle size. *Delamere et al.* [2000] showed in a case study that TOA OLR flux can increase by 20 W m^{-2} in response to changes in r_{ei} from 20 to 140 μm. *Kristjánsson and Kristiansen* [2000] showed that replacing an ice crystal effective radius scheme that assumes a constant value of 30 μm with a temperature-dependent ice effective radius scheme results in changes in longwave cloud forcing up to 12 W m^{-2} in the tropics. Given the impacts of r_{ei} on radiation, it is instructive to evaluate differences in radiation due to uncertainty in the estimation of r_{ei}. To this end, three experiments are conducted (Table 2 and Sections 4.1-4.3). In addition, aerosols can affect the number concentrations of cloud droplets and ice crystals and hence cloud macro- and microphysical properties. Given the large uncertainty in the CAM3 aerosol climatology data, additional SCAM_new runs are conducted to examine how sensitive the simulations are to changes in the number concentrations of cloud droplets and ice crystals due to aerosol effects (Table 2, Section 4.4).

4.1 Ice crystal effective radii in the new and standard schemes

In the standard NCAR CAM3, r_{ei} is prescribed as a function of temperature, ranging from 5 to 220 μm at temperature from 180 to 270K. A modification in the new microphysics parameterization is to calculate r_{ei} as a function of model-predicted ice mass and number concentration. To illustrate the impacts of this modification on the estimation of TOA OLR, we reran the SCAM_new case and replaced r_{ei} by that used in the SCAM_std case. This simulation is called SCAM_exp hereafter (Table 2). The resulting cloud water mixing ratios are not significantly different from those of the control run (i.e., the SCAM_new case). This is, however, not the case for TOA OLR. The difference in TOA OLR between SCAM_exp and SCAM_std is reduced by 50% compared to that between SCAM_new and SCAM_std during the suppressed period (Figure 9a); this suggests that high-level cirrus clouds with low IWC are more transparent to the longwave radiation in the new microphysics scheme than the standard SCAM because of their larger particle sizes, and, therefore, trap less longwave radiation below them. For thicker clouds, as in the monsoon period, the difference in particle size between the two schemes is less important because the infrared emittance is already near 1 for these optically thick clouds.

4.2 Sensitivity to ice crystal effective radius in the new scheme

In the second group of the SCAM_new runs, we multiplied r_{ei} in the new microphysics scheme by a factor for each run. As in the first experiment, TOA OLR is significantly affected during the simulation period, though cloud water mixing ratios are not. Figure 12 (a) compares the TOA OLR values for different runs. Differences in SDLR among the runs are smaller than that in TOA OLR and, therefore, are not shown. Compared to the control run, TOA OLR generally increases with r_{ei}. This is expected because the longwave absorption coefficient of ice crystals is formulated as a function of $1/r_{ei}$. Smaller crystals absorb more longwave radiation. A 20% error in r_{ei} may result in a 5% impact on TOA OLR (by comparing SCAM_80% and SCAM_120% with the control run), which is about 10 W m^{-2} for these conditions. By reducing r_{ei} by 60%, the simulated TOA OLR is reduced by 20% (about 40 W m^{-2}) (by comparing

SCAM_40% and the control run), which is in better agreement with observations. In addition, the effective radii are calculated in SCAM_new based on the assumption that all ice crystals are hexagonal columns [*Liu et al.*, 2007a], which might be unrealistic in some cases. Therefore, these comparisons indirectly test how such an assumption affects simulations.

4.3 Sensitivity to detrained ice particle radius

Cloud water at low altitudes can be brought up to high altitudes through deep convection processes and contributes to ice clouds through the detrainment process. As mentioned in section 2, the contribution of the detrained water to the change rate in ice number concentration is parameterized as $3\rho Q/(4\pi\rho_i r_v^3)$. Determining the volume mean radius r_v for the detrained ice is uncertain. It is taken as a function of temperature in the new scheme used in this study, ranging from 10 to 250 μm in the normal range of temperature (-90 to 0 ºC), while it is taken as a constant value of 32 μm in a recent study by *Morrison and Gettelman* [2008]. Given the uncertainty and importance of detrainment to cirrus clouds, we ran two tests to examine the responses of radiation fields to changes in r_v. The first test run (SCAM_rv=32) is identical to the SCAM_new run except that r_v is set to be 32 μm, which corresponds to the radius value at a temperature of -50 ºC from the temperature-dependent ice radius lookup table prescribed in the NCAR CAM3. The resulting TOA OLR is in general smaller than that from the control run (SCAM_new), especially during the monsoon period when moisture deep convection processes are strong and detrainment occurs mostly below 12 km (Figure 12b). r_v in the control run is larger than 32 μm for detrainment below 12 km (where temperature is about -50 °C), and smaller above 12 km. For a given detrained water amount, the contribution of the detrained water to the rate of increases in ice number concentration increases with decreasing r_v, resulting in larger absorption of the longwave radiation below clouds. This can explain the majority of differences in TOA OLR between the SCAM_rv=32 run and the control run. The second test run (SCAM_80%rv) is identical to the SCAM_new run except that r_v is reduced by a factor of 20%. The resulting TOA OLR is similar to that from the first test run. In the above two test runs, SDLR fluxes are not significantly different from those from the control run.

4.4 Sensitivity to aerosol number concentrations

Several SCAM_new test runs have been made with varying number concentrations of aerosol and cloud particles (the 4th experimental group in Table 2). In the first two runs, the number concentration of ice crystals due to deposition/condensation ice nucleation (N_{dep}) is increased and decreased by a factor of 10, respectively, due to changes in the number concentration of refractive aerosols (e.g., soot and dust). In runs 3 and 4, the ice crystal number concentration from the contact ice freezing of cloud droplets (N_{cont}) is increased and decreased by a factor of 10, respectively, due to changes in the dust number concentration. In runs 5 and 6, the number concentration of cloud droplets (N_d) in the autoconversion of cloud droplets to rain droplets (which is prescribed from the standard CAM3) is increased and decreased respectively by a factor of 2, examining how the new scheme responds to the second indirect effect of aerosols. In the last two runs, cloud droplet effective radius r_{el}, which is used for the radiation calculation and is prescribed from the standard CAM3, is increased and decreased respectively by 20%, examining how the new scheme responds to the first indirect effect of aerosols.

Compared with the SCAM_new control run, cloud fractions from the above 8 test runs are not significantly changed. Differences in other cloud properties and radiation fields between each test run and the control run appear mostly during the monsoon period. Differences in SDLR in most hours are less than 5%, while differences in TOA OLR can reach 20% for optically thick clouds (e.g. 1800UT 23 Jan). No significant correlations between changes in TOA OLR and in r_{el} and the number concentrations of cloud droplets and ice crystals are found. Differences in surface precipitation rate are less than 0.2 mm hr^{-1} in magnitude, with large impacts (percentage change can reach 50%) appearing during some periods of light precipitation. Similar to the radiation fields, changes in surface precipitation rate are not significantly correlated with those in r_{el} and the number concentrations of cloud droplets and ice crystals.

To illustrate changes in cloud microphysical properties due to varying number concentrations of cloud particles, Figure 13 shows the vertical profiles of the differences in LWC, IWC, and FWC between each test run and the control run averaged at the cloudy levels (LWC+IWC > 5 mg m^{-3}) during the monsoon period. For the first two runs (Figures 13a, b, and c), changes in cloud water mixing ratios (LWC, IWC, and FWC) appear at levels within the mixed-phase cloud. As the deposition/condensation ice nucleation increases, IWC and FWC increase but LWC decreases in the mixed-phase cloud, with the maximum changes appearing at 7-8 km above the ground. The relative changes in LWC and IWC can reach 50% due to an increase in deposition/condensation nucleation by a factor of 10. In contrast, changes due to the decrease by the same factor are much smaller, suggesting highly nonlinear responses of LWC and IWC to the deposition/condensation nucleation. LWC, IWC, and FWC respond to changes in the contact freezing (Figure 13d, e and f) in a similar trend as the first two runs except that the decrease and increase in the contact freezing by the same factor result in similar magnitude changes in each of LWC, IWC, and FWC. LWC in the lower-level liquid cloud is also affected due to changes in the contact freezing (Figure 13d). This may be partially because ice particles aloft fall to lower levels with $T > 0$ °C and the melted ice water is added into the liquid cloud.

Changes in LWC within the mixed-phased cloud and lower-level liquid cloud are positively correlated with those in cloud droplet number concentration (Figure 13g), i.e., when cloud droplet number is reduced (increased), autoconversion of droplet to rain speeds up (slows down). Such changes in LWC responding to changes in droplet number concentration are the second indirect effect of aerosols. Figure 13h suggests that an increase (or decrease) in cloud drop number concentration may also result in a slightly increase (decrease) in IWC in the mixed-phase cloud. This is because the contact freezing through the Brownian coagulation increases with the cloud droplet number concentration. In test runs 7 and 8, changes in the droplet effective radius have small changes in cloud water mixing ratio but have similar changes in TOA OLR and SDLR in magnitude (figures not shown), compared with the other six runs.

5. Summary

We have compared cloud properties simulated by the single column version of NCAR CAM3 with a newly-introduced microphysics parameterization scheme and with the standard microphysics parameterization scheme during TWP-ICE. Compared to cloud radar and satellite retrievals, the simulation with either of the schemes can reasonably produce the temporal variations and spatial distributions of clouds. Differences are highlighted as follows. High-level cloud fraction from the simulation with the new scheme is larger than that with the standard scheme, due to the supersaturation with respect to ice being allowed in the new ice scheme. Future model development relating cloud fraction to model-predicted cloud condensate is desirable especially when ice supersaturation is introduced in the model. The magnitudes and vertical distributions of total frozen water (snow plus ice) contents simulated with the two schemes are similar. This is, however, not the case for the ice water content, especially for the mixed-phase clouds. The ice mass fraction in the mixed-phase clouds from the new scheme is larger than that from the standard scheme. The level where ice begins to form in the clouds from the simulation with the new scheme is at 5 km during the monsoon period, which is 2 km lower than that from the simulation with the standard scheme. The ice mass fraction and ice cloud base and top heights simulated with the new scheme are closer to radar and satellite retrievals than those with the standard scheme. The dependence of the frozen water mass fraction on temperature from the new scheme is closer to available observations than that from the standard scheme.

The temporal variations of TOA OLR and SDLR can be reasonably simulated by either of the schemes as well. SDLR values from the simulations with both schemes are similar and in good agreement with observations. In contrast, differences in TOA OLR between the two simulations are marked especially during the suppressed period, due to differences in cloud optical properties such as cloud water path and cloud particle effective radius. A numerical experiment suggests that the different treatments of the ice crystal effective radius can account for 50% of the differences during the suppressed period. Ice clouds simulated with the new scheme are more transparent in the longwave radiation than that with the standard scheme. For thicker clouds, as during the monsoon period, the difference in the ice crystal effective radius is less important for TOA OLR calculation because the infrared emittance is already near 1 for those optically thick clouds. Given the sensitivity of cloud optical properties to the effective radius, experiments are conducted to examine how the uncertainty in the estimation of the ice crystal effective radius affects the calculation of TOA OLR. A 20% uncertainty in r_{ei} may result in a 5% impact of TOA OLR. By reducing r_{ei} by 60%, the simulated TOA OLR is reduced by 20%. SDLR is less affected by the uncertainty in r_{ei}. In addition, we made several sensitivity tests varying the number concentrations of ice crystals due to deposition/condensation ice nucleation and due to the contact freezing of droplets on dust particles as well as droplet number concentration and effective size. Compared with the control run, spatial and temporal distribution patterns of cloud fraction and radiation fields are not significantly affected. Significant changes in LWC, IWC, and TOA OLR in magnitude, however, are found during the monsoon period. These tests show that the simulations with the new scheme can respond reasonably to aerosol effects and also emphasize the importance of correctly simulating aerosols in climate models for aerosol-cloud interactions.

More comparisons are needed, including the following two aspects. First, given the limitations of SCAM that requires accurate large scale advection and tendency, testing the new scheme under the framework of the three-dimensional global CAM3 is desirable. Second, cloud microphysical variables such as ice water mass and ice crystal number concentration need to be compared with in-situ observations.

Acknowledgments:

The authors would like to acknowledge the support from the Department of Energy (DOE) Climate and Environmental Science Division Atmospheric Radiation Measurement program and Climate Change Prediction Program. The Pacific Northwest National Laboratory is operated for the DOE by Battelle Memorial Institute under contract DE-AC06-76RLO 1830. Work at LLNL was performed under the auspices of the U. S. Department of Energy by Lawrence Livermore National Laboratory under contract No. DE-AC52-07NA27344.

Reference:

Allen, G., G. Vaughan, K. N. Bower, P. I. Williams, J. Crosier, M. Flynn, P. Connolly, J. F. Hamilton, J. D. Lee, J. E. Saxton, N. M. Watson, M. Gallagher, H. Coe, J. Allan, T. W. Choularton, and A. C. Lewis (2008), Aerosol and trace-gas measurements in the Darwin area during the wet season, *J. Geophys. Res.*, *113*, DOI: 10.1029/2007JD008706.

Boville, B. A., P. J. Rasch, J. J. Hack, and J. R. McCaa (2006), Representation of Clouds and Precipitation Processes in the Community Atmosphere Model Version 3 (CAM3), *Journal of Climate*, *19*, 2184-2198.

Boyle, J. S., D. Williamson, R. Cederwall, M. Fiorino, J. Hnilo, J. Olson, T. Phillips, G. Potter, and S. Xie (2005), Diagnosis of Community Atmospheric Model 2 (CAM2) in numerical weather forecast configuration at Atmospheric Radiation Measurement sites, *J. Geophys. Res.*, *110*, 1-16.

Clothiaux, E. E., T. P. Ackerman, G. G. Mace, K. P. Moran, R. T. Marchand, M. A. Miller, and B. E. Martner (2000), Objective Determination of Cloud Heights and Radar Reflectivities Using a Combination of Active Remote Sensors at the ARM CART Sites, *Journal of Applied Meteorology*, *39*, 645-665.

Collins, W. D., P. J. Rasch, B. A. Boville, J. J. Hack, J. R. McCaa, D. L. Williamson, B. P. Briegleb, C. M. Bitz, S.-J. Lin, and M. Zhang (2006), The Formulation and Atmospheric Simulation of the Community Atmosphere Model Version 3 (CAM3), *Journal of Climate*, *19*, 2144-2161.

Collins, W. D., P. J. Rasch, B. E. Eaton, B. V. Khattatov, J.-F. Lamarque, and C. S. Zender (2001), Simulating aerosols using a chemical transport model with assimilation of satellite aerosol retrievals: Methodology for INDOEX, *J. Geophys. Res.*, *106*, 7313-7336.

Comstock, J. M., T. P. Ackerman, and G. G. Mace (2002), Ground-based lidar and radar remote sensing of tropical cirrus clouds at Nauru Island: Cloud statistics and radiative impacts, *J. Geophys. Res.*, *107*, 4714.

Comstock, J. M., R. Entremont, D. DeSlover, G. G. Mace, S. Y. Matrosov, S. A. McFarlane, P. Minnis, D. Mitchell, K. Sassen, M. D. Shupe, D. D. Turner, and Z. Wang (2007), An Intercomparison of Microphysical Retrieval Algorithms for Upper-Tropospheric Ice Clouds, *Bulletin of the American Meteorological Society*, *88*, 191-204.

Delamere, J. S., E. J. E. J. Mlawer, and S. A. Clough (2000), The Impact of Cloud Optical Properties on Longwave Radiation in the Arctic, paper presented at Tenth ARM Science Team Meeting Proceedings, San Antonio, Texas, March 13-17, 2000.

Ecuyer, T. S., and G. L. Stephens (2007), The Tropical Atmospheric Energy Budget from the TRMM Perspective. Part II: Evaluating GCM Representations of the Sensitivity of Regional Energy and Water Cycles to the 1998-99 ENSO Cycle, *Journal of Climate*, *20*, 4548-4571.

Field, P. R., R. J. Hogan, P. R. A. Brown, A. J. Illingworth, T. W. Choularton, and R. J. Cotton (2005), Parameterization of ice-particle size distributions for mid-latitude stratiform cloud, *Quarterly Journal of the Royal Meteorological Society*, *131*, 1997-2017.

Gettelman, A., H. Morrison, and S. J. Ghan (2008), A New Two-Moment Bulk Stratiform Cloud Microphysics Scheme in the Community Atmosphere Model, Version 3 (CAM3). Part II: Single-Column and Global Results, *Journal of Climate*, *21*, 3660-3679.

Gregory, D., and D. Morris (1996), The sensitivity of climate simulations to the specification of mixed phase clouds, *Climate Dynamics*, *12*, 641-651.

Iacobellis, S. F., G. M. McFarquhar, D. L. Mitchell, and R. C. J. Somerville (2003), The Sensitivity of Radiative Fluxes to Parameterized Cloud Microphysics, *Journal of Climate*, *16*, 2979-2996.

Kristjánsson, J. E., and J. Kristiansen (2000), Impact of a new scheme for optical properties of ice crystals on climates of two GCMs, *J. Geophys. Res.*, *105*, 10063-10079.

Liao, L., and K. Sassen (1994), Investigation of relationships between Ka-band radar reflectivity and ice and liquid water content, *Atmos. Res.*, *34*, 299–313.

Liu, C.-L., and A. J. Illingworth (2000), Toward More Accurate Retrievals of Ice Water Content from Radar Measurements of Clouds, *Journal of Applied Meteorology*, *39*, 1130-1146.

Liu, X., and J. E. Penner (2005), Ice nucleation parameterization for global models, *Meteor. Z.*, *14*, 499-514.

Liu, X., J. E. Penner, S. J. Ghan, and M. Wang (2007a), Inclusion of Ice Microphysics in the NCAR Community Atmospheric Model Version 3 (CAM3), *Journal of Climate*, *20*, 4526-4547.

Liu, X., S. Xie, and S. J. Ghan (2007b), Evaluation of a new mixed-phase cloud microphysics parameterization with CAM3 single-column model and M-PACE observations, *Geophys. Res. Lett.*, *34*, 1-6.

Lohmann, U. (2002), Possible aerosol effects on ice clouds via contact nucleation, *Journal of the Atmospheric Sciences*, *59*, 647-656.

Mather, J. H., S. A. McFarlane, M. A. Miller, and K. L. Johnson (2007), Cloud properties and associated radiative heating rates in the tropical western Pacific, *J. Geophys. Res.*, *112*, D05201.

May, P. T., J. H. Mather, G. Vaughan, and C. Jakob (2008), FIELD RESEARCH: Characterizing Oceanic Convective Cloud Systems, *Bulletin of the American Meteorological Society*, *89*, 153-155.

Meyers, M. P., P. J. DeMott, and W. R. Cotton (1992), New Primary Ice-Nucleation Parameterizations in an Explicit Cloud Model, *Journal of Applied Meteorology*, *31*, 708-721.

Minikin, A., A. Petzold, J. Ström, R. Krejci, M. Seifert, P. van Velthoven, H. Schlager, and U. Schumann (2003), Aircraft observations of the upper tropospheric fine particle aerosol in the Northern and Southern Hemispheres at midlatitudes, *Geophys. Res. Lett.*, *30*, DOI: 10.1029/2002GL016458.

Morrison, H., and A. Gettelman (2008), A New Two-Moment Bulk Stratiform Cloud Microphysics Scheme in the Community Atmosphere Model, Version 3 (CAM3). Part I: Description and Numerical Tests, *Journal of Climate*, *21*, 3642-3659.

Rasch, P. J., W. D. Collins, and B. E. Eaton (2001), Understanding the Indian Ocean Experiment (INDOEX) aerosol distributions with an aerosol assimilation, *J. Geophys. Res.*, *106*, 7337-7356.

Rasch, P. J., and J. E. Kristjánsson (1998), A Comparison of the CCM3 Model Climate Using Diagnosed and Predicted Condensate Parameterizations, *Journal of Climate*, *11*, 1587-1614.

Rotstayn, L. D., B. F. Ryan, and J. J. Katzfey (2000), A Scheme for Calculation of the Liquid Fraction in Mixed-Phase Stratiform Clouds in Large-Scale Models, *Monthly Weather Review*, *128*, 1070-1088.

Seo, E.-K., and G. Liu (2005), Retrievals of cloud ice water path by combining ground cloud radar and satellite high-frequency microwave measurements near the ARM SGP site, *Journal of Geophys. Res.*, *110*, D14203, doi: 14210.11029/12004JD005727.

Seo, E.-K., and G. Liu (2006), Determination of 3D Cloud Ice Water Contents by Combining Multiple Data Sources from Satellite, Ground Radar, and a Numerical Model, *Journal of Applied Meteorology and Climatology*, *45*, 1494-1504.

Stith, J. L., J. A. Haggerty, A. Heymsfield, and C. A. Grainger (2004), Microphysical Characteristics of Tropical Updrafts in Clean Conditions, *Journal of Applied Meteorology*, *43*, 779-794.

Wu, X., and M. W. Moncrieff (2001), Long-Term Behavior of Cloud Systems in TOGA COARE and Their Interactions with Radiative and Surface Processes. Part III: Effects on the Energy Budget and SST, *Journal of the Atmospheric Sciences*, *58*, 1155-1168.

Xie, S., T. Hume, C. Jakob, S. A. Klein, R. McCoy, and M. Zhang (2009), Observed large-scale structures and diabatic heating and Drying profiles during TWP-ICE, *submitted to Journal of Climate*.

Xie, S., J. Boyle, S. A. Klein, X. Liu, and S. Ghan (2008), Simulations of Arctic mixed-phase clouds in forecasts with CAM3 and AM2 for M-PACE, *J. Geophys. Res.*, *113*, D04211 doi:04210.01029/02007JD009225.

Xie, S., and M. Zhang (2000), Impact of the convection triggering function on single-column model simulations, *J. Geophys. Res.*, *105*, 14983-14996.

Xie, S., M. Zhang, J. Boyle, R. T. Caderwall, G. L. Potter, and W. Lin (2004), Impact of a revised convective triggering mechanism on Community Atmosphere Model, Version 2, simulations: Results from short-range weather forecasts, *J. Geophys. Res.*, *109*, D14102, doi:14110.11029/12004JD004692.

Young, K. C. (1974), The Role of Contact Nucleation in Ice Phase Initiation in Clouds, *Journal of the Atmospheric Sciences*, *31*, 768-776.

Zhang, G. J., and N. A. McFarlane (1995), Sensitivity of climate simulations to the parameterization of cumulus convection in the Canadian Climate Centre General circulation model, *Atmosphere-Ocean*, *33*, 407-446.

Zhang, M., W. Lin, C. B. Bretherton, J. J. Hack, and P. J. Rasch (2003), A modified formulation of fractional stratiform condensation rate in the NCAR Community Atmosphere Model (CAM2), *J. Geophys. Res.*, *108*, 4035, doi:4010.1029/2002JD002523.

Zhang, M. H., and J. L. Lin (1997), Constrained Variational Analysis of Sounding Data Based on Column-Integrated Budgets of Mass, Heat, Moisture, and Momentum: Approach and Application to ARM Measurements, *Journal of the Atmospheric Sciences*, *54*, 1503-1524.

Zhang, M. H., J. L. Lin, R. T. Cederwall, J. J. Yio, and S. C. Xie (2001), Objective Analysis of ARM IOP Data: Method and Sensitivity, *Monthly Weather Review*, *129*, 295-311.

Zhang, M. H., W. Y. Lin, S. A. Klein, J. T. Bacmeister, S. Bony, R. T. Cederwall, A. D. D. Genio, J. J. Hack, N. G. Loeb, U. Lohmann, P. Minnis, I. Musat, R. Pincus, P. Stier, M. J. Suarez, M. J. Webb, J. B. Wu, S. C. Xie, M. S. Yao, and J. H. Zhang (2005), Comparing clouds and their seasonal variations in 10 atmospheric general circulation models with satellite measurements, *J. Geophys. Res.*, *110*, 1-18.

Caption:

Figure 1 A sketch of TWP-ICE site and instrument deployment around the Darwin site (131ºE, 12ºS, northern Australia). Source: http://www.arm.gov

Figure 2 Time series of the precipitation rate from ground-based observations and from model outputs for the monsoon period (left of the dotted line) and suppressed period (right side of the dotted line). Universal time is used.

Figure 3 (a) Time-height distribution of the frequency of occurrence of clouds from ARSCL, (b) cloud fraction from the SCAM_std run, (c) cloud fraction from the SCAM_new run.

Figure 4 (a) Time-height distribution of the liquid water mixing ratio simulated from SCAM_std, (b) SCAM_new, and (c) all available cloud radar retrievals (data gaps are shaded by gray areas). Gray contours are temperature in °C.

Figure 5 Time series of the liquid water path from the SCAM_std run and the SCAM_new run (lines), and from MWR (triangles). MWR retrievals are shown only during non-precipitating periods.

Figure 6 (a) time-height distribution of the frozen water (sum of snow and ice) mixing ratio from SCAM_std, (b) SCAM_new, (c) Satellite retrievals, and (d) all available cloud radar retrievals (data gaps are shaded by gray areas). Gray contours are temperature in °C.

Figure 7 Time series of ice water path from SCAM_std, SCAM_new, and from satellite retrievals and cloud radar retrievals. Note that, snow mixing ratio has been included into the IWP calculation for comparisons with observations.

Figure 8 (a) Time-height distribution of the ice water mixing ratio simulated from SCAM_std, and (b) SCAM_new. Gray contours are temperature in °C.

Figure 9 Vertical profiles of the median values of ice water mixing ratios from SCAM_std and SCAM_new. Red lines are for frozen water (ice plus snow) mixing ratio.

Figure 10 (a) Joint frequency distribution of temperature and fractional ice water content in the mixed phase cloud from SCAM_std, (b) from SCAM_new. Snow content has been included into ice content. Red diamonds denote the average f_{ice} for given a temperature interval. Black triangle and asterisk are derived from field observations [*Field et al.*, 2005] by *Gettelman et al.* [2008].

Figure 11 (a) TOA OLR simulated from SCAM_std, SCAM_new, and retrieved from satellite observations. (b) Surface downward longwave radiation. The dashed green line denotes results from SCAM_exp, where the effective radius of ice crystals in SCAM_new is imposed to be equal to that used in SCAM_std.

Figure 12 (a) TOA OLR from the 2nd experimental group (Table 2), where the effective radius of ice crystals is equal to 40%, 80%, and 120% of that in the control run (SCAM_new). Black dotted line denotes TOA OLR from satellite retrievals. (b) The 3rd experiment group. SCAM_80%rv: ice volume mean r_v in the detrained water is equal to 80% of that in the control run; SCAM_rv=32: r_v is imposed to a constant value of 32 μm.

Figure 13 Vertical profiles of mean differences in LWC, IWC, and FWC between each of SCAM_new runs in experimental group 4 (Table 2) and the control run during the monsoon period. (a), (b), and (c) are for SCAM_new runs of varying number concentrations of ice crystals due to deposition/condensation ice nucleation. (d), (e), and (f) are for the SCAM_new runs of varying number concentrations of ice crystals due to contact freezing. (g), (h), and (i) are for the SCAM_new runs of varying cloud droplet number concentrations.

Table 1 Comparisons of mean LWP and IWP, and their standard deviations (g m^{-2}).

Periods	Variable	SCAM_std	SCAM_new	MMCR or MWR	Satellite
Monsoon	LWP [a]	319±62	202±42	56±8	NA
	IWP [a]	126±36	148±46	23±5	47±30
	IWP [b]	394±63	369±58	#	480±108
suppressed	LWP [a]	161±19	170±22	40±5	NA
	IWP [a]	13±2	7.5±1	5±1.5	1.5±1

Note: a: only for non-precipitating hours (precipitation rate from the ground-based observations < 0.2mm hr^{-1}); b: for all hours. NA: not available. [#] Retrievals are not reliable when precipitation occurs and, therefore, not shown. IWP is from MMCR. LWP is from MWR.

Table 2 Summary of experiments.

Experimental group	run identity	Description
I	Control	Same as SCAM_new
	SCAM_exp	Same as SCAM_new, but r_{ei} is replaced by that used in the standard SCAM.
II	SCAM_40%	r_{ei} = 40% r_{ei0}
	SCAM_80%	r_{ei} = 80% r_{ei0}
	SCAM_120%	r_{ei} = 120% r_{ei0}
III	SCAM_rv=32	Detrained ice particle radius r_v = 32 um
	SCAM_80%rv	Detrained ice particle radius r_v= 80% r_{v0}
IV	(1) SCAM_0.1Ndp0	$N_{dep}=0.1N_{dep0}$
	(2) SCAM_10Ndp0	$N_{dep}=10N_{dep0}$
	(3) SCAM_0.1Nct0	$N_{cont}=0.1N_{cont0}$
	(4) SCAM_10Nct0	$N_{cont}=10N_{cont0}$
	(5) SCAM_0.5Nd0	$N_d=0.5N_{d0}$
	(6) SCAM_2Nd0	$N_d=2N_{d0}$
	(7) SCAM_80%rel0	r_{el}=80% r_{el0}
	(8) SCAM_120%rel0	r_{el}=120% r_{el0}

Note: r_{ei0} and r_{el0} represent the ice crystal and droplet effective radii used in the control run, respectively. r_{v0} is the volume mean radius for the detrained water used in the control run. In group IV, N_{dep} is the number concentration of ice crystals due to deposition /condensation in the mixed-phase cloud, N_{cont} is the number concentration of ice crystals due to the contact freezing of cloud droplets, and N_{d0} is the number concentration of cloud droplets. The subscript '0' signifies the value used the control run. r_{el} is the droplet effective radius.

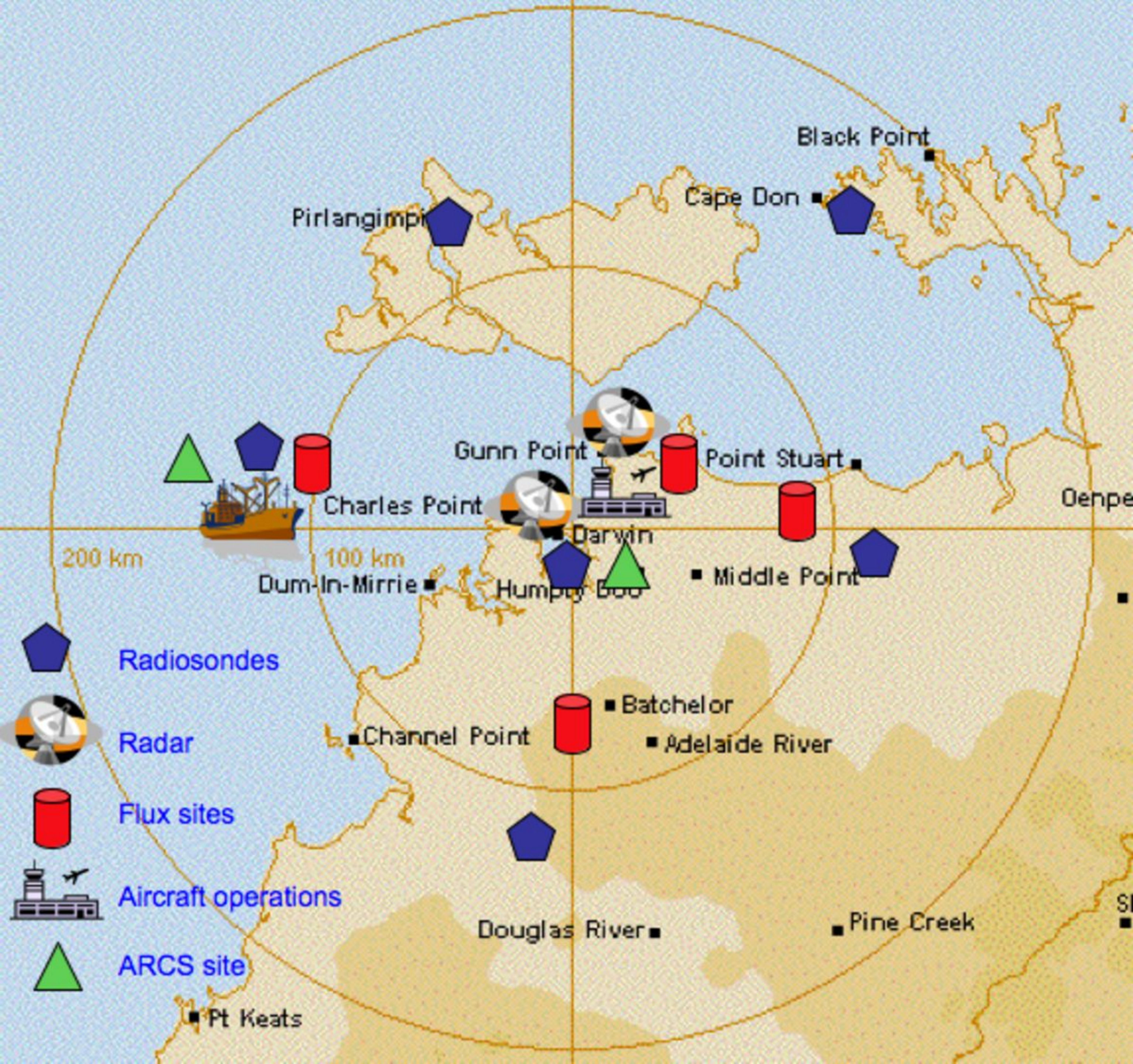

Black Point
Cape Don
Pirlangimpi
Gunn Point
Point Stuart
Charles Point
Darwin
Oenpe
200 km
100 km
Dum-In-Mirrie
Humpty Doo
Middle Point
Radiosondes
Radar
Batchelor
Channel Point
Adelaide River
Flux sites
Aircraft operations
Douglas River
Pine Creek
ARCS site
Pt Keats

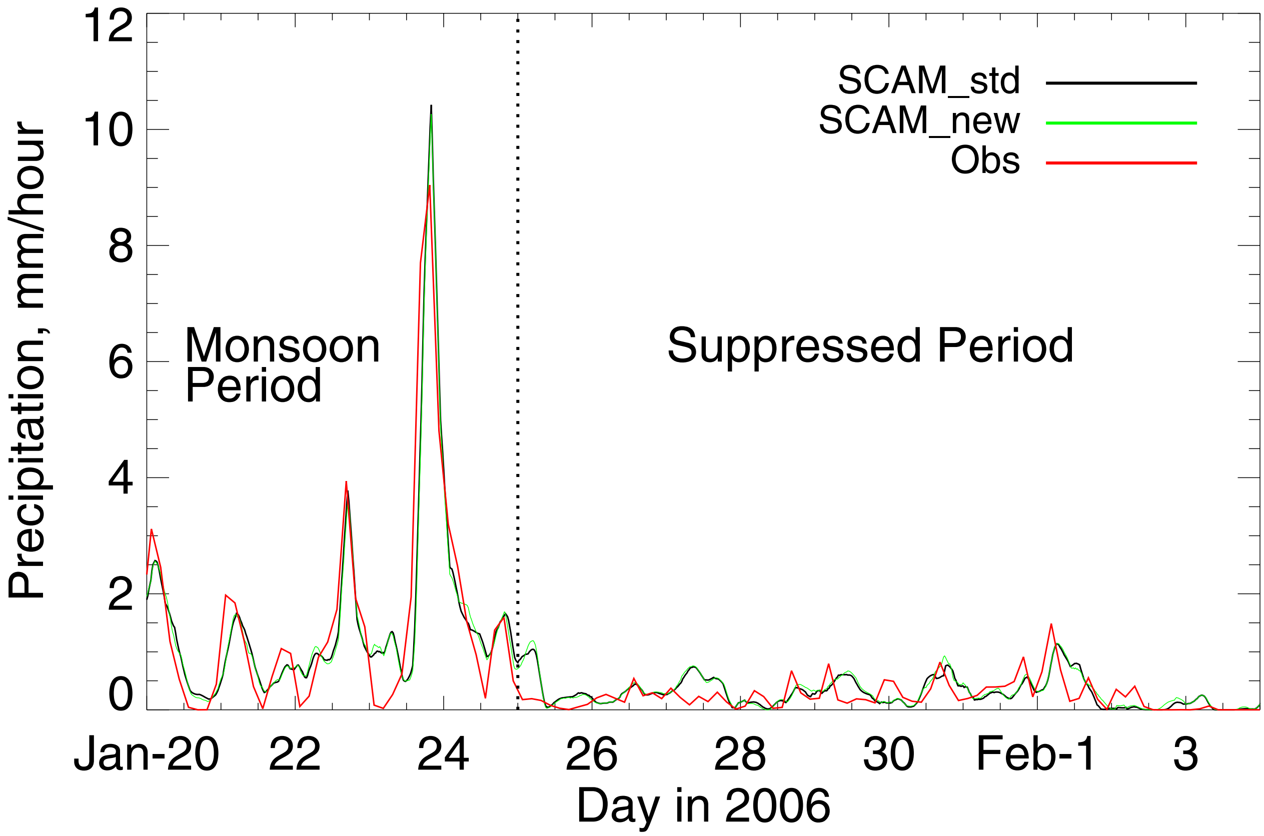

SCAM_std
SCAM_new
Obs
Monsoon
Period
Suppressed Period
Precipitation, mm/hour
0
2
4
6
8
10
12
Jan-20
22
24
26
28
30
Feb-1
3
Day in 2006

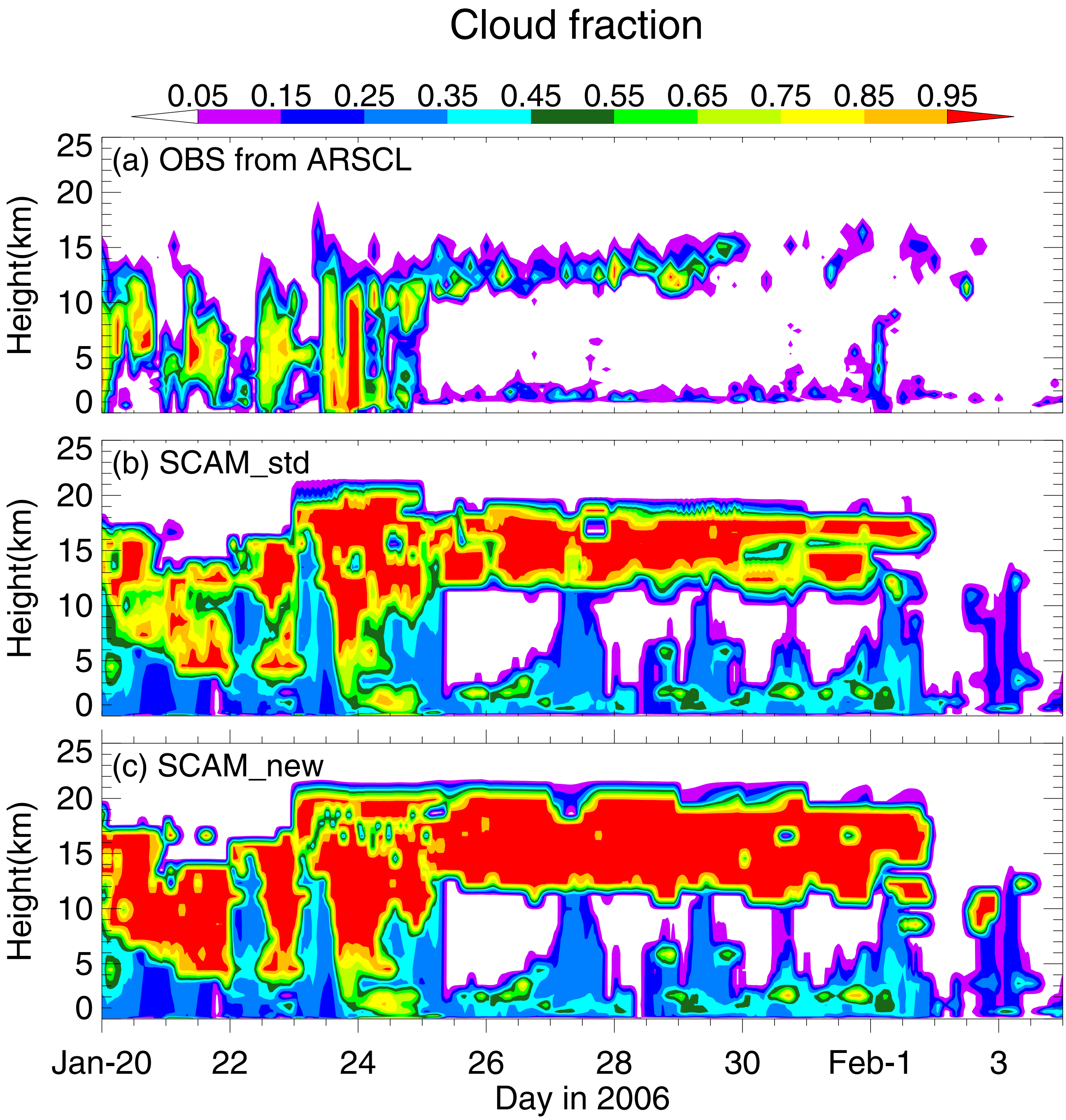

Cloud fraction
0.05 0.15 0.25 0.35 0.45 0.55 0.65 0.75 0.85 0.95
(a) OBS from ARSCL
(b) SCAM_std
(c) SCAM_new
Height(km)
0 5 10 15 20 25
Jan-20 22 24 26 28 30 Feb-1 3
Day in 2006

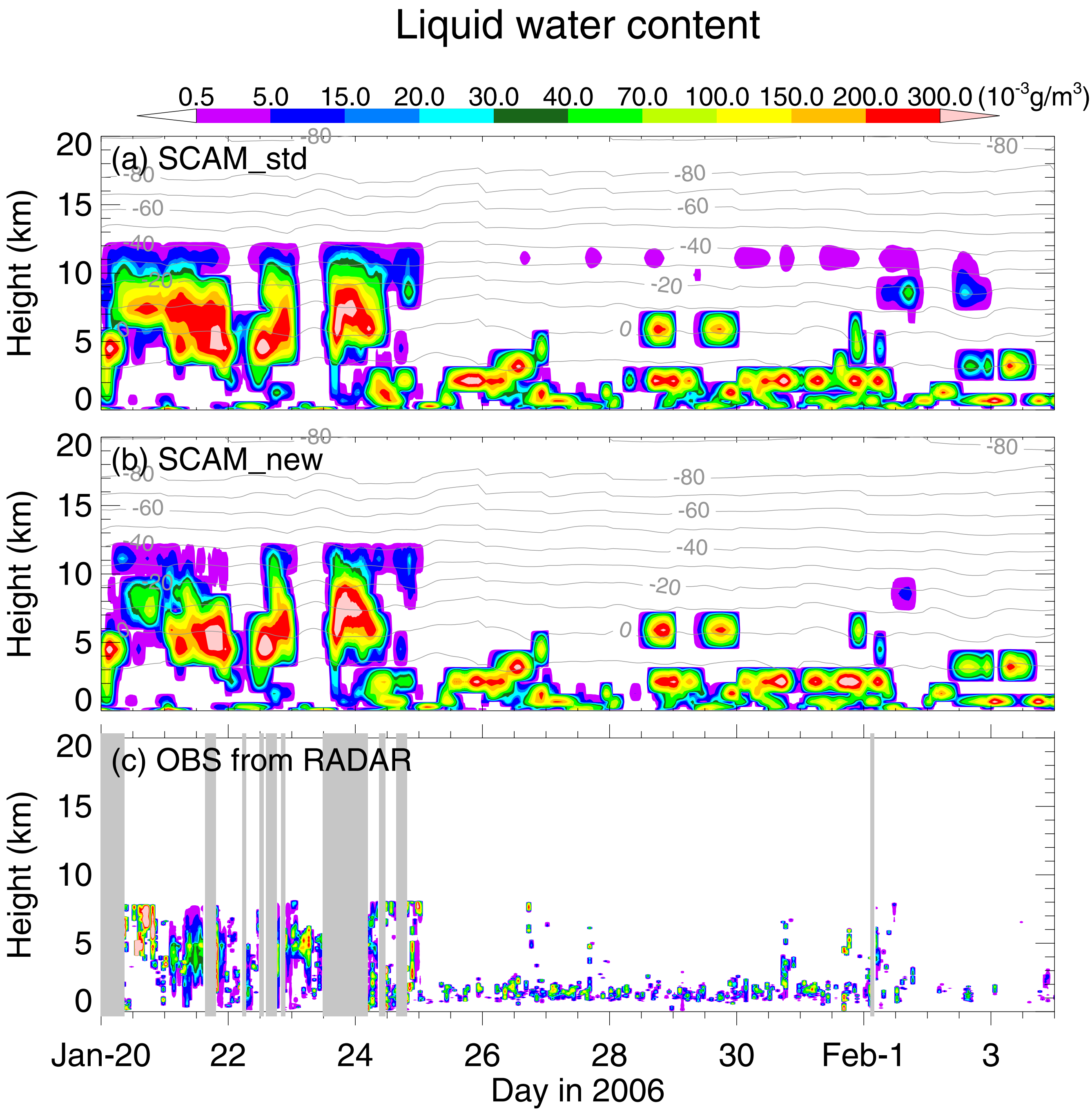
Liquid water content
0.5 5.0 15.0 20.0 30.0 40.0 70.0 100.0 150.0 200.0 300.0 (10^-3 g/m^3)
(a) SCAM_std
(b) SCAM_new
(c) OBS from RADAR
Height (km)
Jan-20 22 24 26 28 30 Feb-1 3
Day in 2006

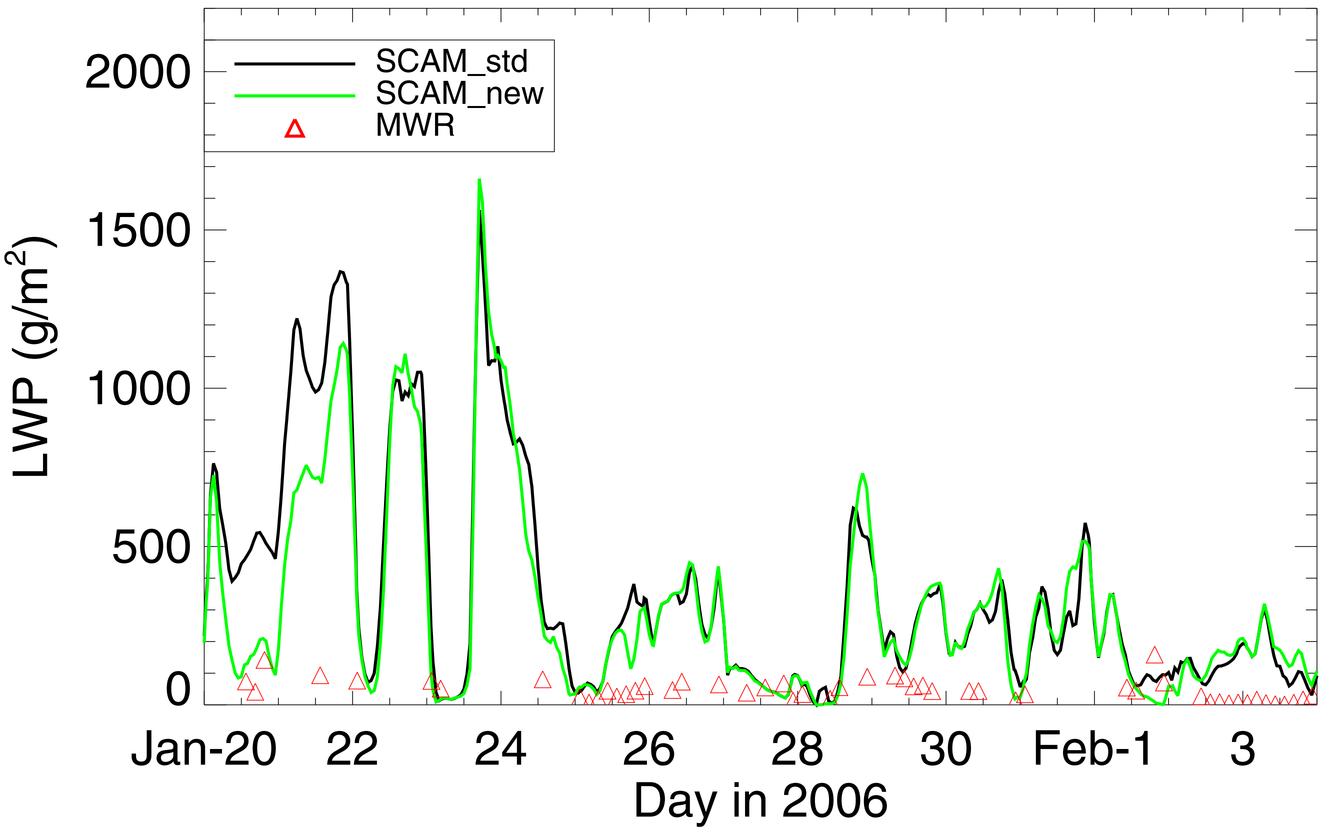

SCAM_std
SCAM_new
MWR
LWP (g/m^2)
2000
1500
1000
500
0
Jan-20
22
24
26
28
30
Feb-1
3
Day in 2006

Frozen water content

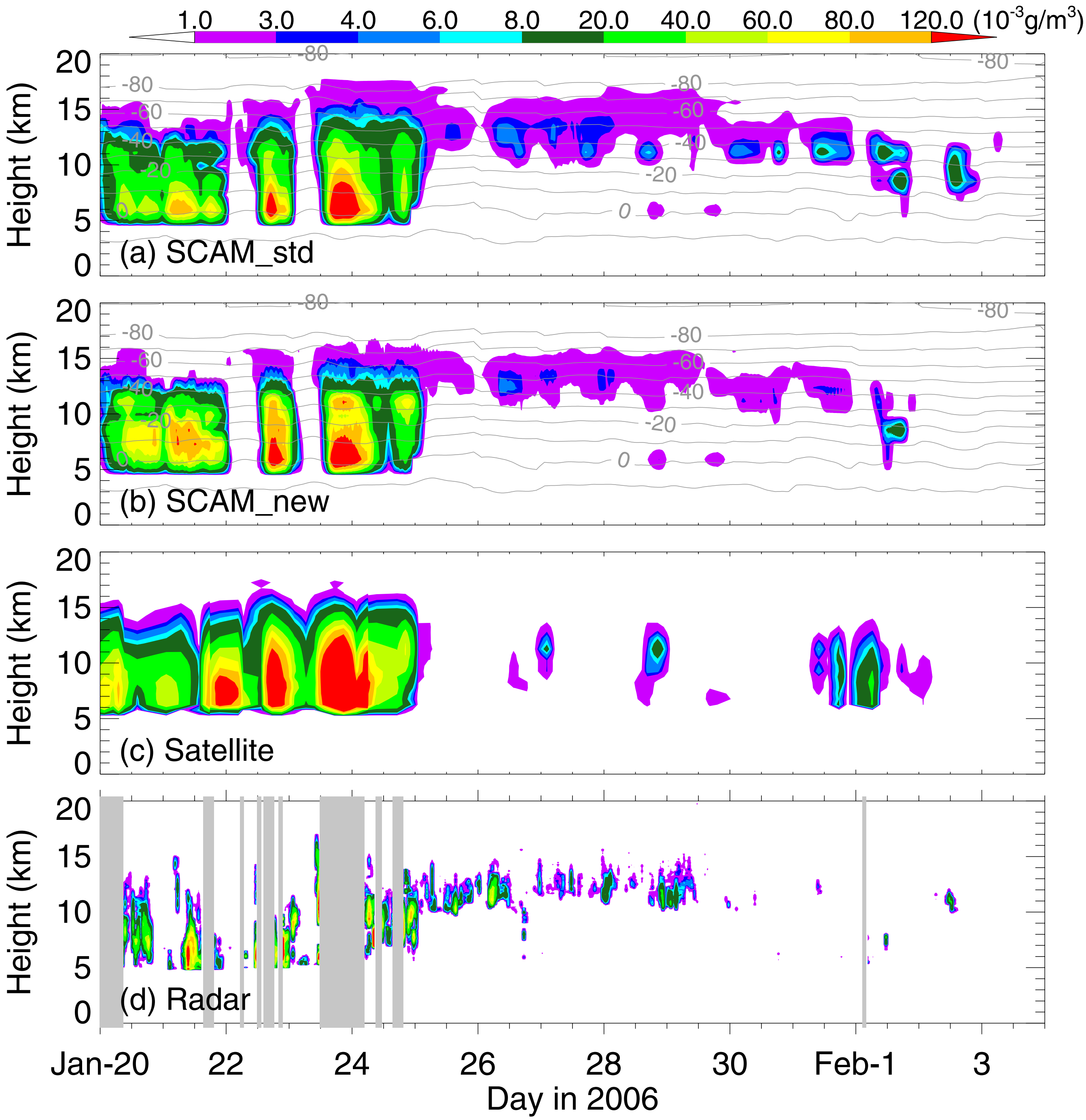

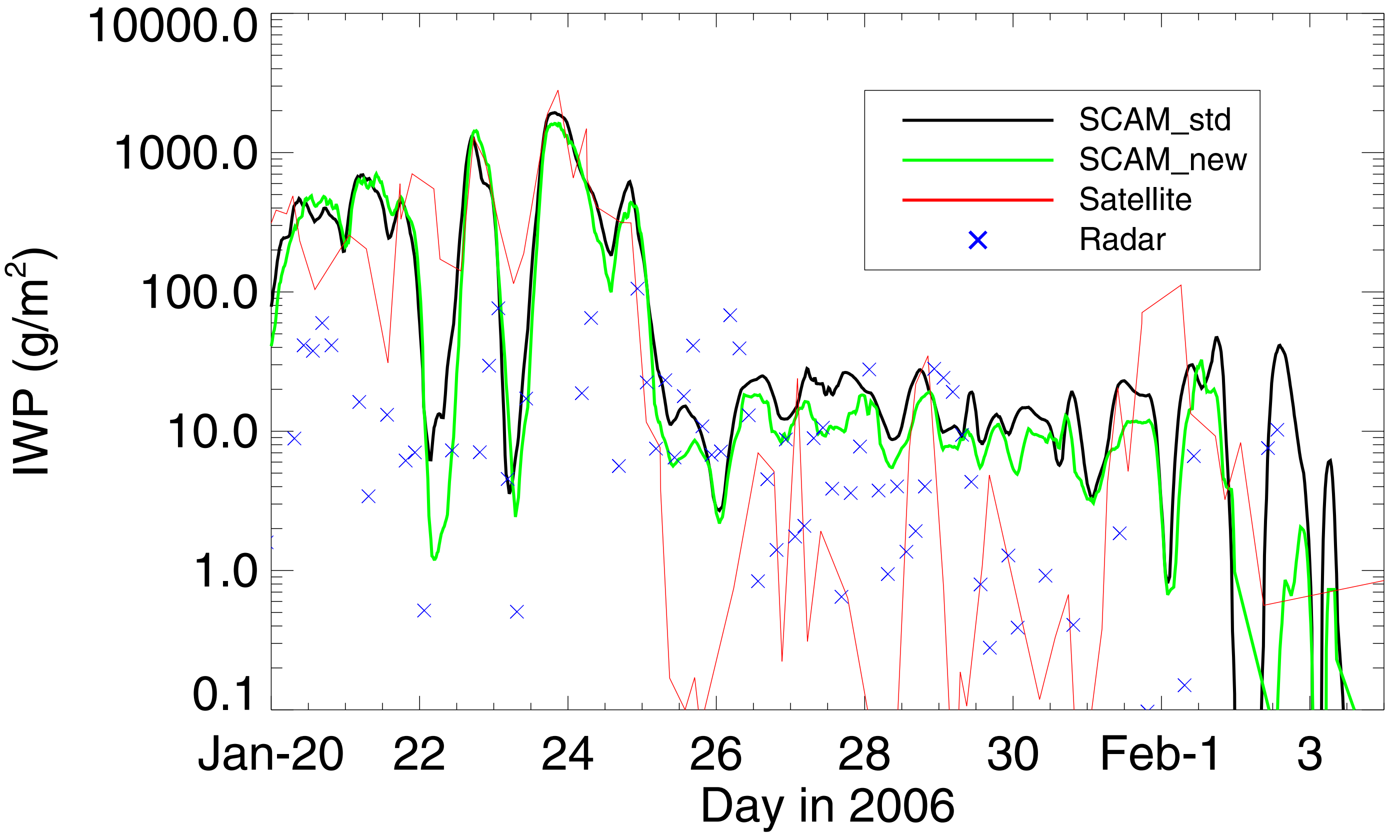

IWP (g/m^2)
10000.0
1000.0
100.0
10.0
1.0
0.1
SCAM_std
SCAM_new
Satellite
Radar
Jan-20
22
24
26
28
30
Feb-1
3
Day in 2006

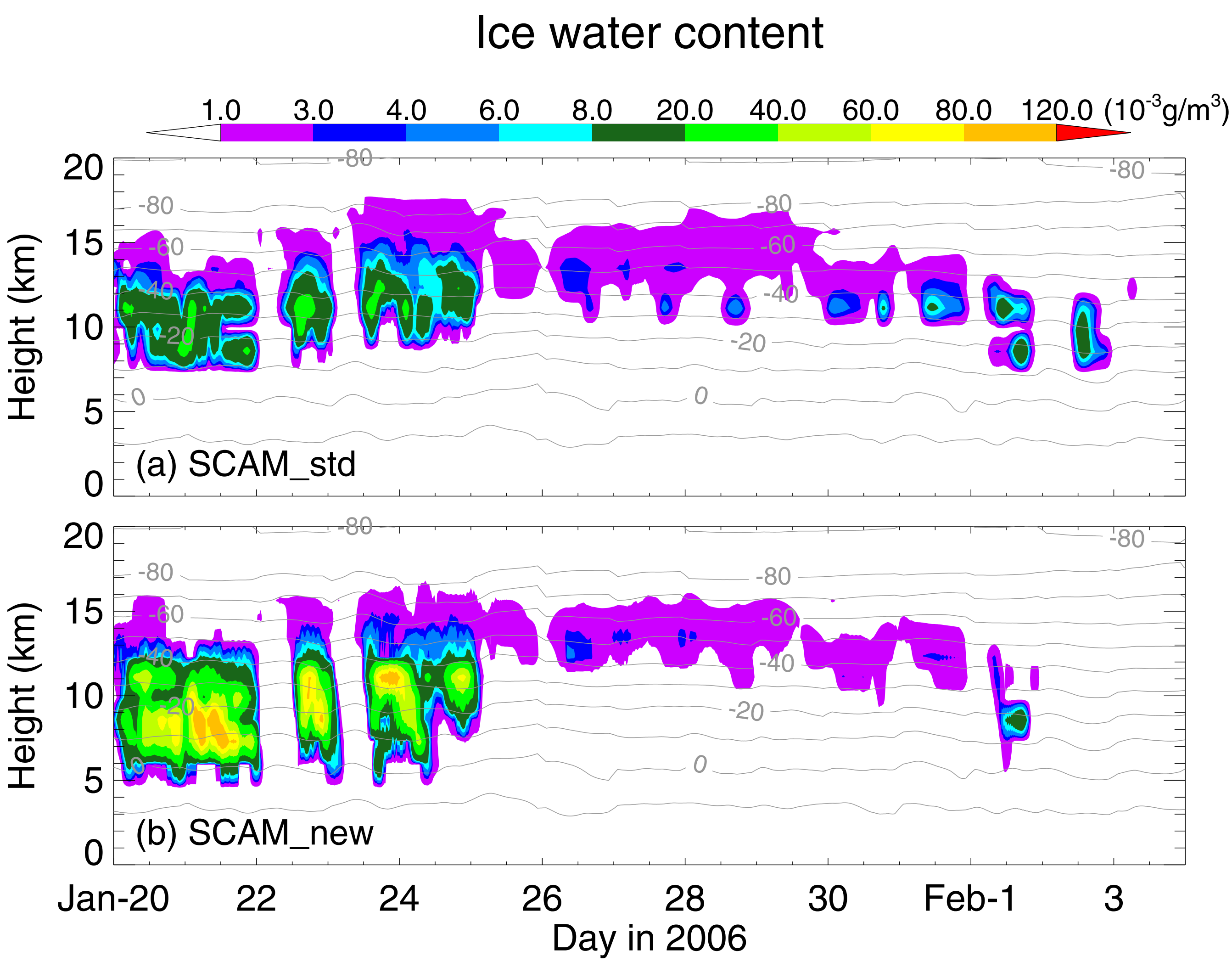

Ice water content
1.0
3.0
4.0
6.0
8.0
20.0
40.0
60.0
80.0
120.0
(10^-3g/m^3)
Height (km)
(a) SCAM_std
(b) SCAM_new
Jan-20
22
24
26
28
30
Feb-1
3
Day in 2006

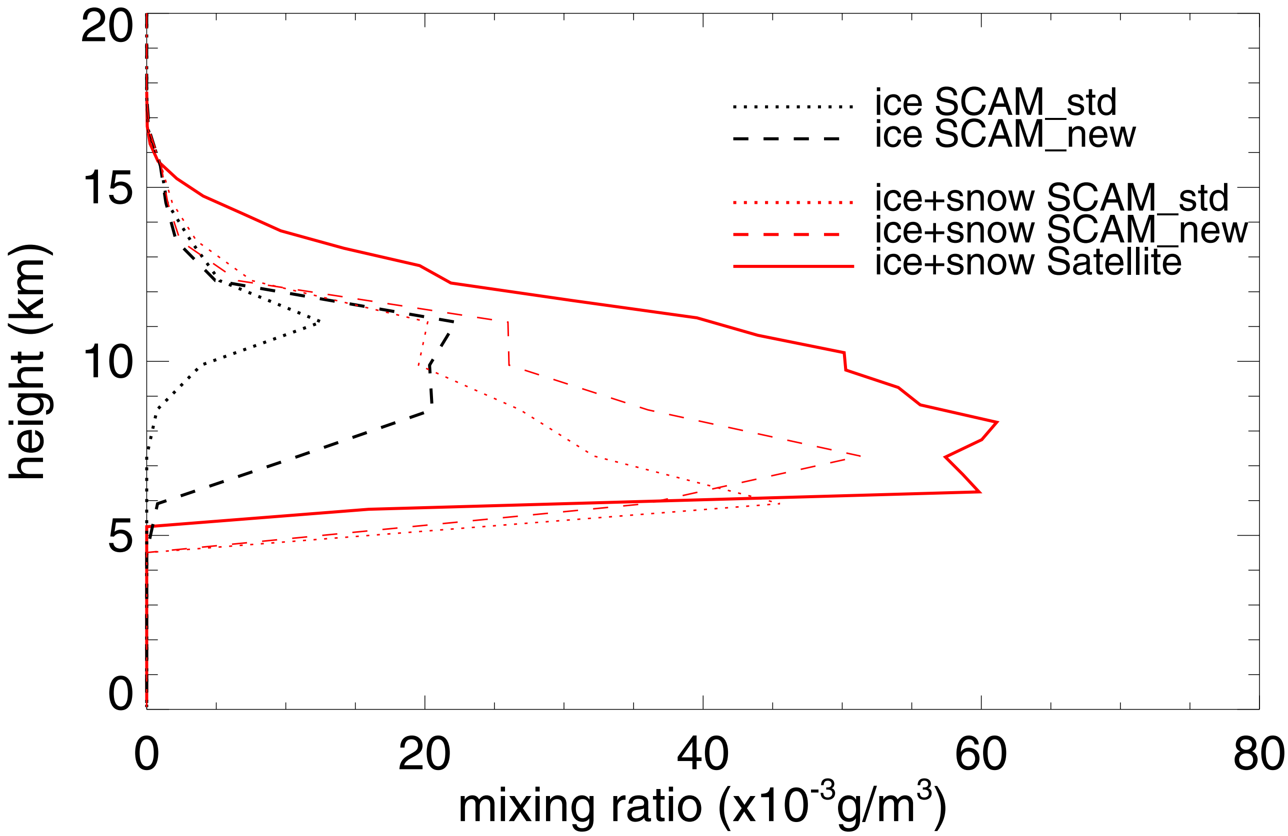

ice SCAM_std
ice SCAM_new
ice+snow SCAM_std
ice+snow SCAM_new
ice+snow Satellite
height (km)
mixing ratio (x10-3g/m3)
0
5
10
15
20
0
20
40
60
80

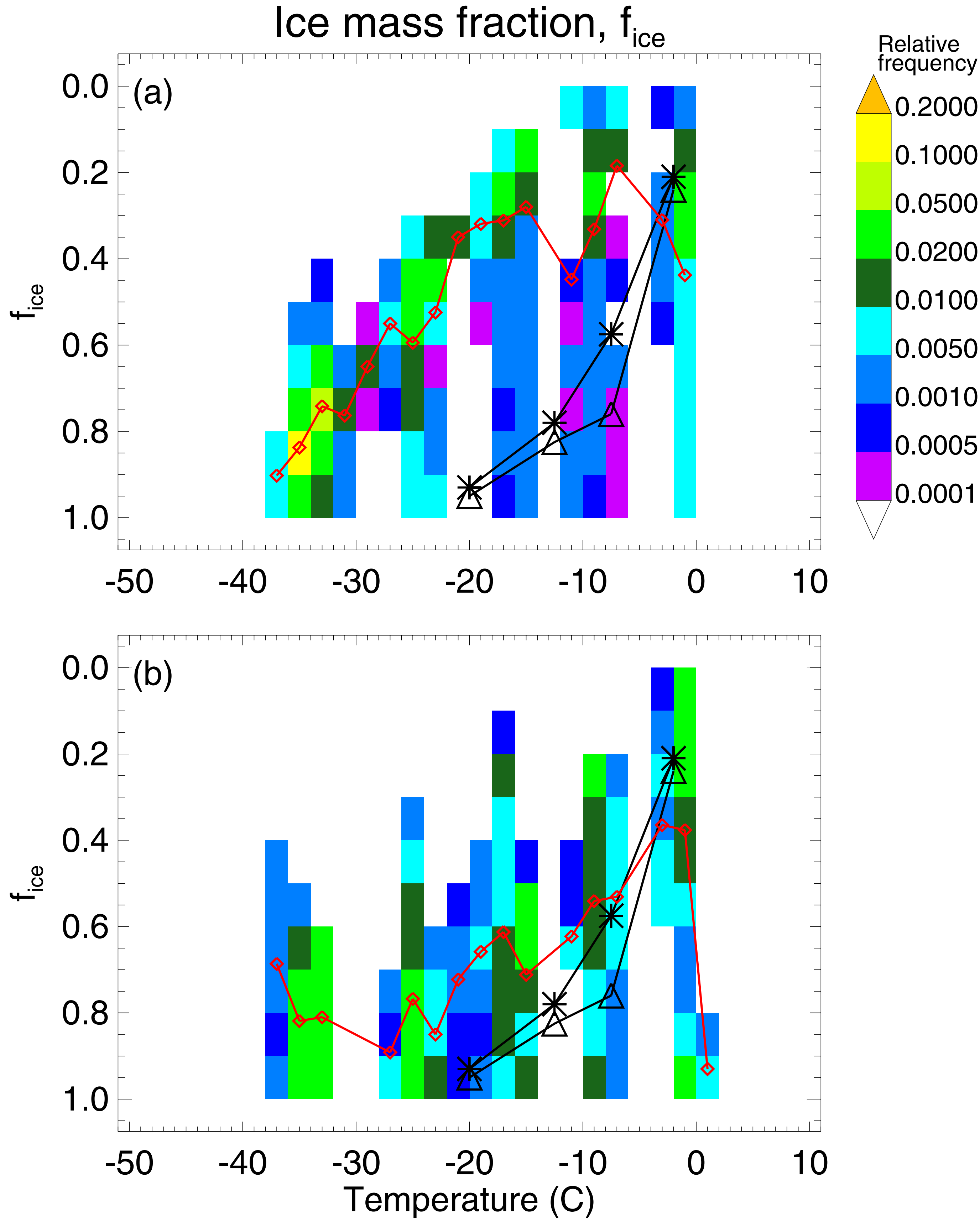

Ice mass fraction, f_{ice}
(a)
(b)
f_{ice}
0.0
0.2
0.4
0.6
0.8
1.0
-50
-40
-30
-20
-10
0
10
Temperature (C)
Relative frequency
0.2000
0.1000
0.0500
0.0200
0.0100
0.0050
0.0010
0.0005
0.0001

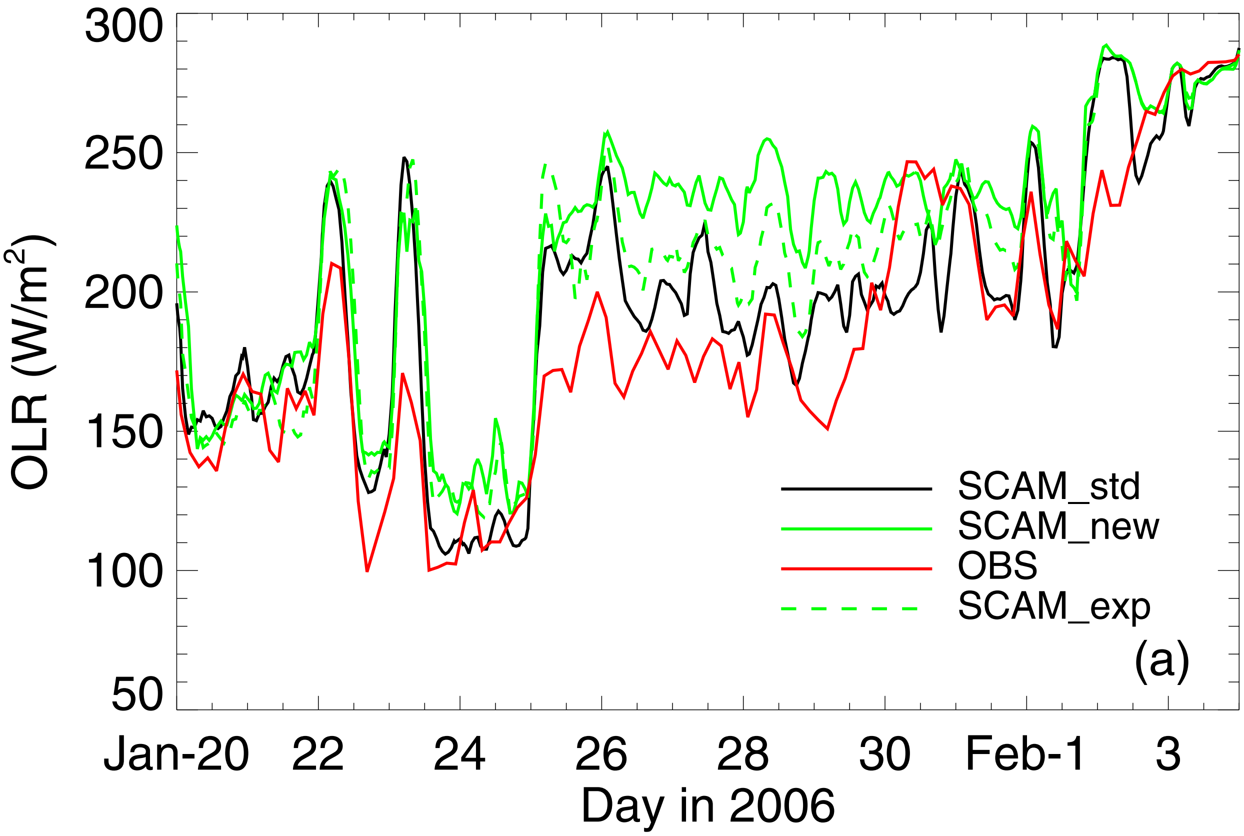
300
250
200
150
100
50
OLR (W/m2)
SCAM_std
SCAM_new
OBS
SCAM_exp
(a)
Jan-20
22
24
26
28
30
Feb-1
3
Day in 2006

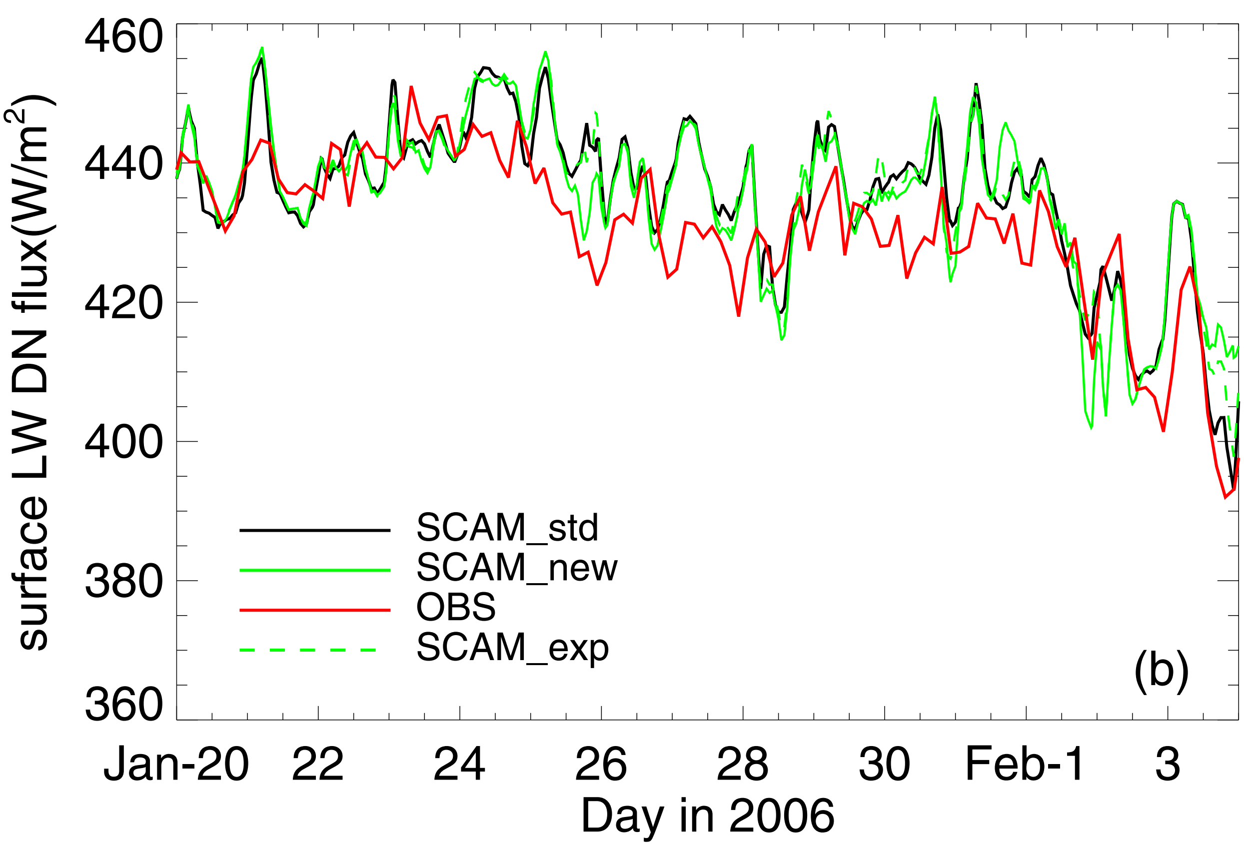
460
440
420
400
380
360
surface LW DN flux(W/m2)
SCAM_std
SCAM_new
OBS
SCAM_exp
(b)
Jan-20
22
24
26
28
30
Feb-1
3
Day in 2006

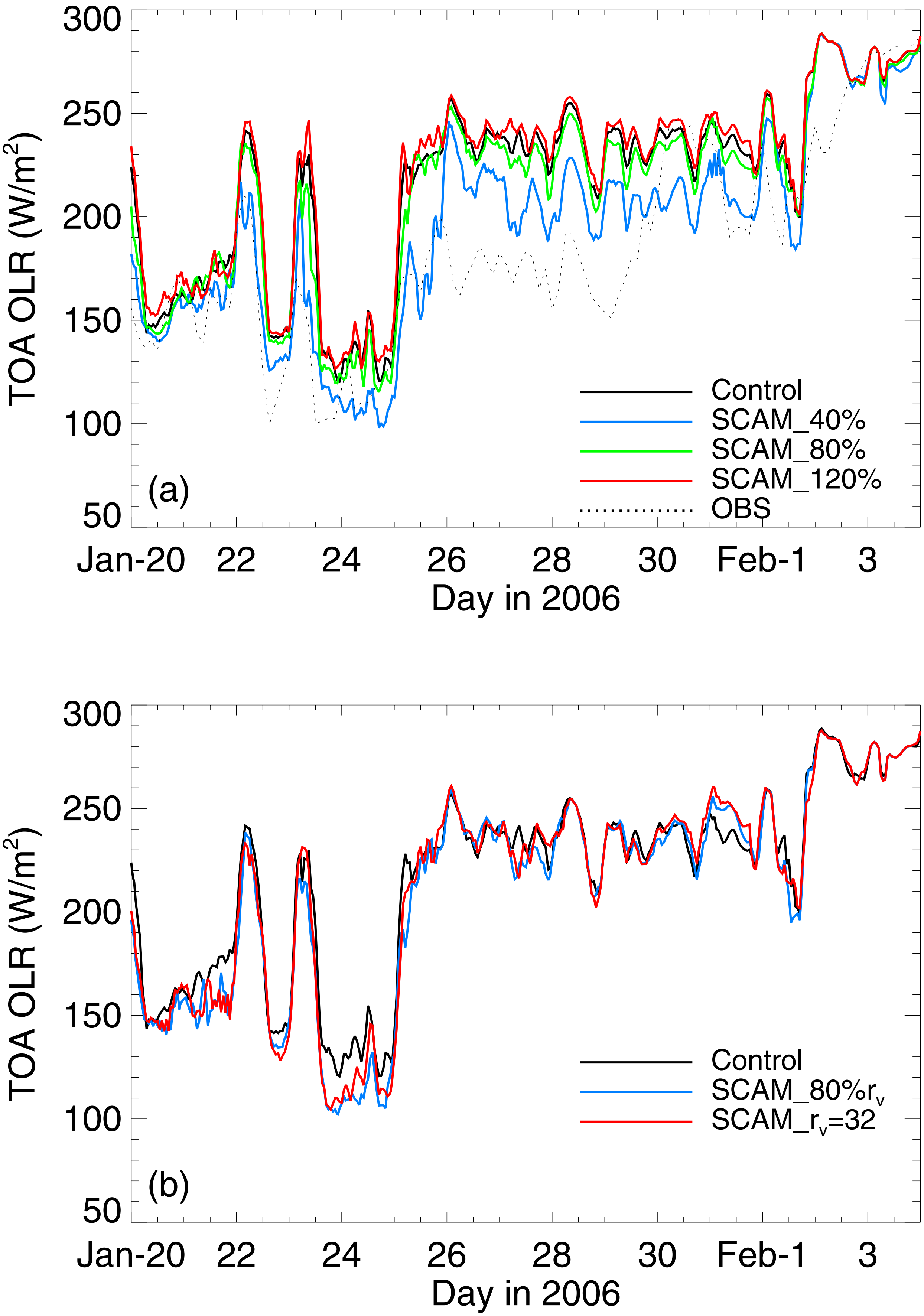

TOA OLR (W/m2)
300
250
200
150
100
50
(a)
Control
SCAM_40%
SCAM_80%
SCAM_120%
OBS
Jan-20
22
24
26
28
30
Feb-1
3
Day in 2006
(b)
Control
SCAM_80%rv
SCAM_rv=32

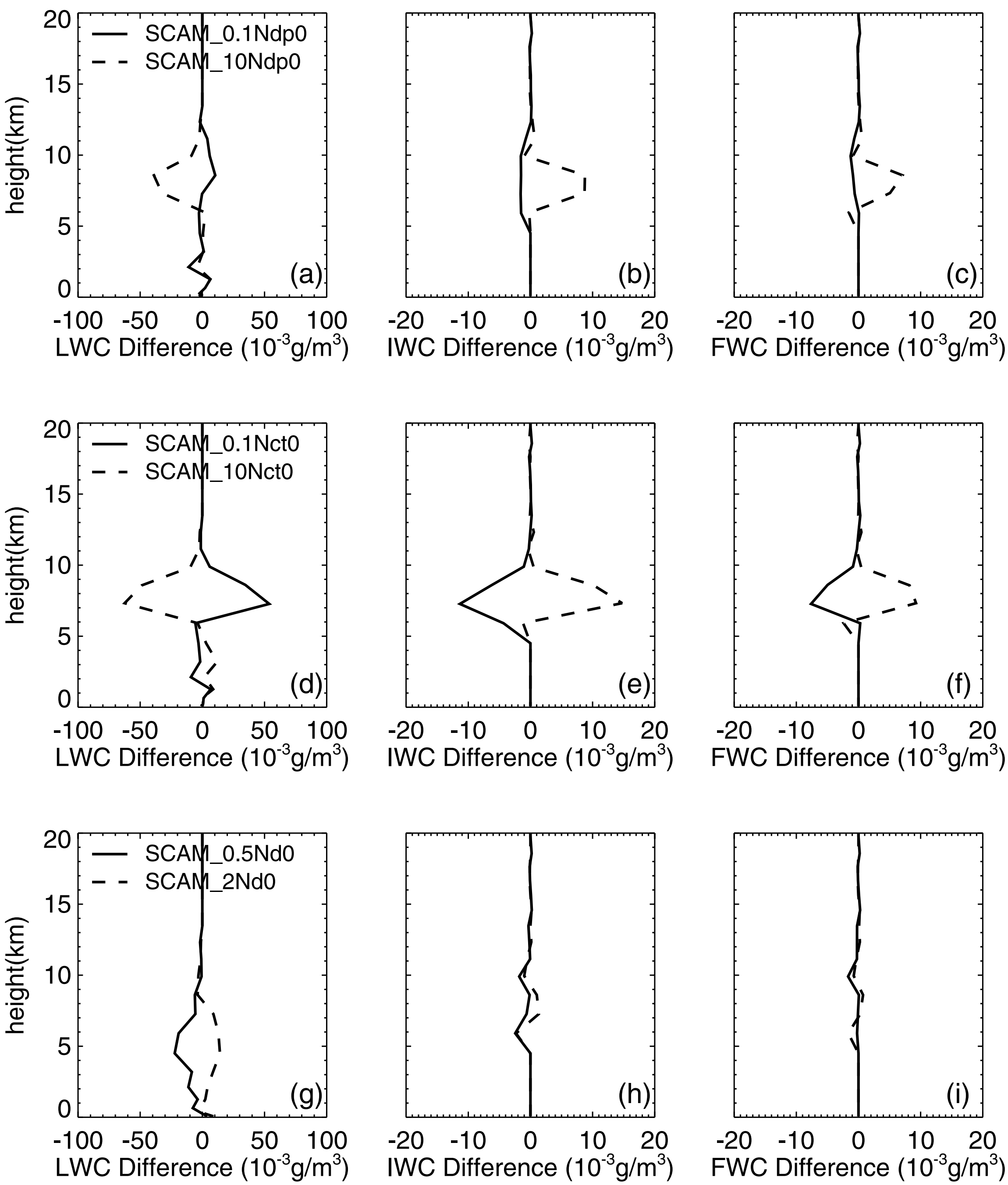
SCAM_0.1Ndp0
SCAM_10Ndp0
SCAM_0.1Nct0
SCAM_10Nct0
SCAM_0.5Nd0
SCAM_2Nd0
height(km)
LWC Difference (10^{-3}g/m^3)
IWC Difference (10^{-3}g/m^3)
FWC Difference (10^{-3}g/m^3)
(a)
(b)
(c)
(d)
(e)
(f)
(g)
(h)
(i)